Chapter 1　Introduction

1.1 Background

Photonic crystals are artificial microstructures in which the refractive index is periodically modulated at a length scale comparable to the wavelength of operation [1, 2]. For specific crystal configurations, this index periodicity can lead to a complete photonic bandgap (in a certain range of frequencies), thus inhibiting wave propagation in all three directions [1]. As noted in several studies, the presence of gaps in the macroscopic dispersion relation of such periodic structures introduces novel features that one can exploit to control the propagation of light. In this respect, photonic crystals are highly promising in terms of integrating useful optical components such as waveguides, couplers, cavities, and filters on the same substrate [2]. Interest is especially focused on the electromagnetic (EM) wave being guided within the waveguide by the mechanism of band-gap confinement. The PCWs are the most promising elements of photonic crystals for building large-scale photonic integrated circuits, because the EM waves can be transmitted [3], sharply bent [4], split [5], and dispersion compensated [6] by means of specific PCW designs.

Modulation instability (MI) is a general feature of discrete as well as continuum nonlinear wave equations. For this instability, a specific range of wave numbers of plane-wave profiles of the form $u(x, t) \sim \exp(i(kx - \omega t))$ becomes unstable to modulations, leading to an exponential growth of the unstable modes and eventually to delocalization (upon excitation of such wave numbers) in momentum space. That is equivalent to localization in position space, and hence the formation of localized, coherent solitary wave structures [7]. The realizations of this instability span a diverse set of disciplines, ranging from fluid dynamics [8] (where it is usually referred to as the Benjamin–Feir instability) and nonlinear optics [9, 10] to plasma physics [11]. One of the earliest contexts in which its significance was appreciated was the linear stability analysis of deep water waves [8, 12]. It was recognized much later that the conditions for MI would be significantly modified for discrete settings relevant to, for instance, the local denaturation of DNA [13] or coupled arrays of optical waveguides [14, 15]. In the latter case, a relevant model is the discrete nonlinear Schrödinger equation (DNLS) [16], and its MI conditions were discussed in [17].

Optical solitons are self-trapped light beams or pulses that are supported by a balance between diffraction (or dispersion) and various nonlinearities. The existence of optical spatial solitons was suggested by Chiao et al. in 1964 [18]. They proposed that an optical beam might be able to prevent the different effect and preserve the beam shape when the optical beam propagates in a nonlinear medium under special intensity and beam width. The optical temporal solitons were predicted by Hasegawa and Tappert [19] in 1973 and first observed experimentally by Mollenauer, Stolen and Gordon [20] in 1980. An optical pulse is a wave-packet composed of many frequency components. When it propagates in a dispersive linear medium, the pulse envelope will broaden because the various frequency components are caused by different refraction indices and therefore travel at different phase velocities. A commonly used method to prevent the longitudinal spatial spreading of an optical pulse due to dispersion is by utilizing the self-phase modulation resulted from the optical Kerr effect of the medium [21,22]. Optical temporal solitons in optical fibers have been studied thoroughly theoretically and experimentally in the last three decades because they are suitable for long distance optical telecommunication application [23].

1.2 Motivation

Recently, a new type of optical waveguide that involves a periodic sequence of coupled high-Q resonators was proposed [24, 25]. In such a system, waveguiding is accomplished via light hopping or tunneling among successive microcavities that effectively act as defects within the crystal. Interestingly, this process has much in common with electronic transport in crystalline solids when it is described within the so-called tight-binding approximation [24–28]. Optical wave propagation in both linear and χ^2 nonlinear coupled-resonator optical waveguides has also been investigated [29, 30]. Of course, like any other waveguides, including those in photonic crystals [31], coupled resonator optical waveguides are dispersive elements and can thus cause significant pulse broadening during propagation. These group-velocity dispersion effects are of course expected to be more pronounced for relatively short pulses (i.e., when the pulse occupies only a few cavities). Therefore, it will be of interest to find ways to counteract dispersive effects in such systems [32, 33].

In this thesis, we want to show that spatiotemporal discrete solitons can propagate undistorted along a chain of coupled nonlinear high-Q cavities or defects that are embedded in a photonic crystal structure. Such states are possible as a result of the balance between the effects of discrete lattice dispersion with that of material nonlinearity. In order to know how large the magnitude of nonlinear coefficient should be needed, we must discuss what conditions can produce modulation instability [34, 35] to make the perturbation become unstable in nonlinear PCWs primarily. Then, with these conforming situations, the dispersion will be redeemed and the solitons will be formed. Therefore, we explore the properties of PCW via the coupling of point defects under the tight-binding approximation [36], which assumes that the field distribution (or wave function) of an individual point defect is strongly localized around this point defect. The dispersive behavior of a single PCW can be described by the coupling with the neighboring point-defect modes. Diverse defect lines that we design will have different dispersive relation. According to the dispersive relation we get, we can incident wave with appropriate wave vectors and frequencies to create solitons in different nonlinear coefficients.

1.3 Organization of the thesis

In this thesis, we divided the text into four chapters. We introduce the brief review of photonic crystal waveguides and its applications. Besides, we have narrated a brief statement of modulation instability (MI) and solitons to the background and our research motivations in first chapter. In Chapter 2, we expound the normal theory of MI and soliton propagation in photonic crystal waveguides first. Then, we apply the tight-binding theory to derive a new extended nonlinear Schrödinger equation to describe the MI and soliton propagation in PCWs with nonlinear line defects. We also briefly introduce the simulation of fourth order Runge-Kutta method finally. After that, we compare our simulation results with analytic solutions to discuss the modulation instability and soliton propagation in PCWs with nonlinear line defects in Chapter 3. In the end, the final conclusion and future works will be presented in Chapter 4.

Chapter 2 Theory and Calculation Method

2.1 Soliton-- nonlinear Schrödinger equation

The main equation governing the evolution of optical fields in a nonlinear medium is known as the nonlinear Schrödinger equation (NLS). We outline the derivation of the NLS equation for a CW beam propagating inside a nonlinear optical medium with Kerr (or cubic) nonlinearity. The Maxwell equation can be used to obtain the following wave equation for the electric field associated with an optical wave propagating in such a medium [40]:

$$\nabla^2 E-\frac{1}{c^2}\frac{\partial^2 E}{\partial t^2}=\frac{1}{\varepsilon_0 c^2}\frac{\partial^2 P}{\partial t^2}, \tag{2.1}$$

where c is the speed of light in vacuum permittivity. The induced polarization P consists of two parts such that

$$P(r,t)=P_L(r,t)+P_{NL}(r,t), \tag{2.2}$$

where the linear part P_L and the nonlinear part P_{NL} are related to the electric field by the general relations [37]-[39]

$$P_L(r,t)=\varepsilon_0\int_{-\infty}^{\infty}\chi^{(1)}(t-t')\cdot E(r,t')dt', \tag{2.3}$$

$$P_{NL}(r,t)=\varepsilon_0\iiint\chi^{(3)}(t-t_1,t-t_2,t-t_3)\times E(r,t_1)E(r,t_2)E(r,t_3)dt_1dt_2dt_3, \tag{2.4}$$

where $\chi^{(1)}$ and $\chi^{(3)}$ are the first- and third-order susceptibility tensors. These relations are valid in the electric-dipole approximation under assumption that the medium response is local. They also neglect the second-order nonlinear effects, assuming that the medium has an inversion symmetry.

Even when only the lowest-order nonlinear effects are included, Eq. (2.4) is too complicated to be useful. Considerable simplification occurs if the nonlinear response is assumed to be instantaneous so that the time dependence of $\chi^{(3)}$ is given by the produce of three delta functions of the form $\delta(t- t_1)$. Equation (2.4) then reduces to

$$P(r,t) = \varepsilon_0 \chi^{(3)} E(r,t)E(r,t)E(r,t)\,. \tag{2.5}$$

The assumption of instantaneous nonlinear response amounts to neglecting the contribution of molecular vibrations to $\chi^{(3)}$ (the Raman effect).

Several other simplifying assumptions are necessary. First, P_{NL} can be treated as a small perturbation to P_L because nonlinear changes in the refractive index are $\Delta n/n < 10^{-6}$ in practice. Second, the optical field is assumed to maintain its polarization along the fiber length so that a scalar approach can be used. Third, the optical field is assumed to be quasi-monochromatic. In the slowly varying envelope approximation, it is useful to separate the rapidly varying part of the electric field by writing it in the form

$$E(r,t) = \frac{1}{2}\hat{x}[E(r,t)\exp(-i\omega_0 t) + c.c.]\,, \tag{2.6}$$

where ω_0 is the carrier frequency, $\hat{x}$ is the polarization unit vector, and *E(r, t)* is a slowly varying function of time (relative to the optical period). The polarization components P_L and P_{NL} can also be expressed in a similar way.

When Eq. (2.6) is substituted in Eq. (2.5), $P_{NL}(r, t)$ is found to have a term oscillating at ω_0 and another term oscillating at the third-harmonic frequency, $3\omega_0$. The latter term requires phase matching and is generally negligible. The slowly varying part $P_{NL}(r, t)$ of the nonlinear polarization is then given by

$$P_{NL}(r,t) \approx \varepsilon_0 \varepsilon_{NL} E(r,t), \tag{2.7}$$

where the nonlinear contribution to the dielectric constant is defined as

$$P_{NL}(r,t) \approx \varepsilon_0 \varepsilon_{NL} E(r,t), \tag{2.8}$$

The linear part of the polarization can be written from Eq. (2.3) as $P_L=\varepsilon_0\,\chi_{xx}^{(1)}$ E. In fact, the linear and nonlinear parts can be combined to provide the following expression for the dielectric constant [40]

$$\tilde{\varepsilon}(\omega) = 1 + \chi_{xx}^{(1)}(\omega) + \varepsilon_{NL}, \tag{2.9}$$

where a tilde denote the Fourier transform of the quantity under it. The dielectric constant can be used to define the refractive index $\tilde{n}$ and the absorption coefficient $\tilde{\alpha}$. However, both $\tilde{n}$ and $\tilde{\alpha}$ become intensity dependent because of ε_{NL}. It is customary to introduce

$$\tilde{n} = n_0 + n_2 |E|^2, \quad \tilde{\alpha} = \alpha + \alpha_2 |E|^2. \tag{2.10}$$

The linear index n_0 and the absorption coefficient α are related to the real and imaginary parts of $\tilde{\chi}^{(1)}_{xx}$. Using $\varepsilon = (\tilde{n} + i\tilde{\alpha}c/2\omega_0)^2$ and Eq. (2.8) and (2.9), the nonlinear, or Kerr, coefficient n_2 and the two-photon absorption coefficient α_2 are given by

$$n_2 = \frac{3}{8n}\mathrm{Re}(\chi^{(3)}_{xxx}),$$

$$\alpha_2 = \frac{3\omega_0}{4nc}\mathrm{Im}(\chi^{(3)}_{xxx}), \tag{2.11}$$

where Re and Im stand for the real and imaginary parts, respectively.

The nonlinear medium for which the third-order susceptibility dominates and Eq. (2.10) describes the nonlinear response accurately is referred to as the Kerr medium. High-order nonlinear effects can be included in a phenomenological manner by using $\tilde{n} = n_0 + n_{nl}(I)$ in place of Eq. (2.10), where $n_{nl}(I)$ represents the nonlinear part of the refractive index that depends in the beam intensity $I=|E|^2$. In the case of a Kerr medium, $n_{nl}(I)=n_2I$.

To discuss pulse propagation in optical fiber, we should start from Eq. (2.1) and the pulse envelope is now time dependent and can be written as

$$E(r,t) = A(Z,t)F(X,Y)\exp(i\beta_0 Z), \tag{2.12}$$

where *F(X,Y)* is the transverse field distribution associated with the fundamental mode of the single-mode fiber. The time dependent of *A(Z,t)* implies that all spectral components of the pulse may not propagate at the same speed inside an optical fiber because of the chromatic dispersion. This effect is included by modifying the refractive index in Eq. (2.10) as

$$\tilde{n} = n(\omega) + n_2 |E|^2 . \tag{2.13}$$

The frequency dependence of $n(\omega)$ plays an important role in the formation of temporal solitons. It leads to broadening of optical pulses in the absence of the nonlinear effects.

Our aim is to obtain an equation satisfied by the pulse amplitude $A(Z,t)$. It is useful to work in the Fourier domain for including the effects of chromatic dispersion and to treat the nonlinear term as a small perturbation. The Fourier transform $\tilde{A}(Z,\omega)$ is found to satisfy [40]

$$\frac{\partial \tilde{A}}{\partial Z} = i[\beta(\omega) + \Delta\beta - \beta_0]\tilde{A} , \tag{2.14}$$

where $\beta(\omega) = k_0 n(\omega)$ and $\Delta\beta$ is the nonlinear part, defined as

$$\Delta\beta = k_0 n_2 |A|^2 \frac{\iint |F(x,y)|^4 \, dxdy}{\iint |F(x,y)|^2 \, dxdy} \equiv \gamma |A|^2 . \tag{2.15}$$

The physical meaning of Eq. (2.14) is clear. Each spectral component within the pulse envelope acquires, as it propagates down the fiber, a phase shift whose magnitude is both frequency and intensity dependent.

We can go back to the time domain by taking the inverse Fourier transform of Eq. (2.14) functional form of $\beta(\omega)$ is rarely know, it is useful to expand $\beta(\omega)$ in a Taylor series around the carrier frequency ω_0 as

$$\beta(\omega)=\beta_0+(\omega-\omega_0)\beta_1+\frac{1}{2}(\omega-\omega_0)^2\beta_2+\frac{1}{6}(\omega-\omega_0)^3\beta_3+\dots, \qquad (2.16)$$

where

$$\beta_m=\left(\frac{d^m\beta}{d\omega^m}\right)_{\omega=\omega_0} \qquad (m=1,\ 2,\ \dots). \qquad (2.17)$$

The cubic and high-order terms in this expansion are generally negligible if the pulse spectral width $\Delta\omega \ll \omega_0$. Their neglect is consistent with the quasi-monochromatic approximation used ealier. If $\beta_2 \approx 0$ for some specific values of ω_0 (in the vicinity of the zero-dispersion wavelength of the fiber, for example), it may be necessary to include the cubic term. We substitute Eq. (2.16) into Eq. (2.14) and take the inverse Fourier transform. During the Fourier-transform operation, ω - ω_0 is replaced by the differential operator $i(\partial/\partial t)$. The resultant equation for $A(Z, t)$ becomes

$$\frac{\partial A}{\partial Z}+\beta_1\frac{\partial A}{\partial t}+\frac{i\beta_2}{2}\frac{\partial^2 A}{\partial t^2}=i\gamma\left|A\right|^2 A. \qquad (2.18)$$

The parameters β_1 and β_2 include the effects of dispersion to the first and the second orders, respectively. Physically, $\beta_1 = 1/v_g$, where v_g is the group velocity associated with the pulse and β_2 takes into account the dispersion of group velocity. For this reason, β_2 is called the group-velocity dispersion (GVD) parameter.

Equation (2.18) can be reduced to the (1+1)-dimensional NLS equation, where 1 corresponds to the number of the transverse dimensions in NLS equation and +1 indicates the propagation direction z, by marking the following transformation of variables

$$\tau = (t - \beta_1 Z)/T_0, \quad z = Z/L_D, \quad u = \sqrt{|\gamma| L_D} A\,, \tag{2.19}$$

where T_0 is a temporal scaling parameter (often taken to be the input pulse width) and $L_D = T_0^2/|\beta_2|$ is the dispersion length. The variable x now measures time in the reference frame of the moving pulse. In terms of the these new variable, Eq. (2.18) takes the form

$$i\frac{\partial u}{\partial z} - \frac{s}{2}\frac{\partial^2 u}{\partial \tau^2} \pm |u|^2 u = 0\,, \tag{2.20}$$

where $s = sgn(\beta_2) = \pm 1$ stands for the sign of the GVD parameter. The GVD parameter β_2 can be positive or negative, depending on the wavelength. The nonlinear term is positive for silica fibers but may become negative for waveguides made of semiconductor materials.

2.2 Modulation instability– nonlinear Schrödinger equation

In this section we consider the simplest (1+1)-dimensional NLS equation, describing either the propagation of a CW beam in a planer waveguide or propagation of an optical pulse inside optical fiber, and show that this equation exhibits an instability. This instability is known as the modulation instability because it leads to spatial or temporal modulation of a constant-intensity plane wave.

The NLS equation (2.20), has the simplest solution in the form of an optical pulse

$$u(z,t) = u_0 \exp(ipz + iqt), \tag{2.21}$$

where u_0 is a constant and p and q satisfy the dispersion relation

$$p = -q^2/2 + \mathrm{sgn}(n_2)u_0^2, \tag{2.22}$$

where $sgn(n_2)=\pm1$ depending on the sign of n_2. This solution shows that such a pulse of amplitude u_0 propagates through the nonlinear medium unchanged expect for acquiring an intensity- dependent phase shift.

An important question is whether this temporal solution is stable against small perturbations. The answer is provided by a linear stability analysis of this solution. We follow the standard procedure and look for solutions of the form

$$u = (u_0 + u_1 + iv_1)\exp(ipz + iqt), \tag{2.23}$$

where u_1 and v_1 represent small perturbations. Substituting Eq. (2.23) into the NLS equation (2.20) and linearizing the resultant equations, we obtain a system of two coupled linear equations for u_1 and v_1. Looking for solutions to these functions in the form of plane waves exp($iKz+iQt$), we obtain the dispersion relation

$$K = -qQ \pm Q[sQ^2/4 + u_0^2]^{1/2}, \tag{2.24}$$

where s= sgn(β_2). The pulse solution is stable if perturbations at any wave number Q do not grow with propagation. This is the case as long as K is real.

Equation (2.24) shows that the optical pulse solution, Eq. (2.21), is absolutely stable only in the case of nomal dispersion ($\beta_2 > 0$). Physically, small-amplitude waves can propagate along with the background intense plane wave in the case of anomalous dispersion, although their propagation constant K depends on the pulse intensity u_0^2. The solution, Eq. (2.21), becomes unstable in an anomalous dispersive medium ($\beta_2 < 0$) whenever the pulse intensity is such that $u_0^2 < Q^2/4$. This is the modulation instability.

In temporal case, perturbation with certain values of Q become unstable when the last two terms in the NLS equation, Eq. (2.20) have the same sign. The growth rate g is related to the imaginary part of K and is given by

$$g(Q) = \mathrm{Im}[K(Q)] = |Q|\sqrt{u_0^2 - Q/4}\,. \tag{2.25}$$

This growth rate is also called the modulation instability gain. Figure 2.1 shows the instability gain as a function of perturbation frequency Q for u_0=1 and 2. The gain exists for both positive and negative values of Q in the range $|Q| < 2u_0$. The maximum gain occurs for $Q = \sqrt{2}u_0$ and has the value $g_{max} = u_0^2$. In normal units, the peak gain is related to the intensity of the pulse as $g_{max}=k_0 n_2 I_0$ and remains relatively small until the intensity becomes large. For example, I_0 should exceed 100 MW/cm^2, even for AlGaAs waveguides, known to have a relatively large value of n_2 (see Table 2.1)

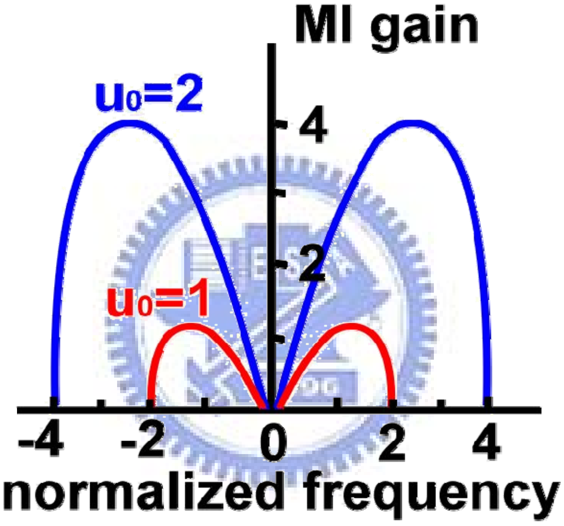

Fig. 2.1 Gain spectrum g(Q) of modulation instability for u_0=1 and 2

Nonlinear Material	Wavelength (μm)	α (cm^{-1})	n_2 (10^{-14} cm^2/W)
SiO2 glass	1.0 ~ 1.6	< 10^{-6}	0.0024
$As_{0.38}S_{0.62}$	1.3 ~ 1.6	0.02	4.2
AlGaAs	1.55	0.1	20
PTS crystal	1.6	0.8	220

Table 2.1 Kerr coefficients for several nonlinear material.

2.3 Dispersion relation by PWEM

Before doing our discussion, we should understand characteristics of the PCW that we used. First, we begin with perfect photonic crystal structure and we can see this structure has it own bandgap in Fig. 2.2. We assume the radiation of the perfect point (or primitive cell) is $0.2D$ and its relative permittivity ε is 12. Next, in order to let light transmit and combing in this bandgap, we try to create a line defect to make some frequency of light can propagate in it. In our design, the defect points are $0.05D$ and this condition can allow most of frequencies passing through within the bandgap. According to these conditions, we can get an dispersion relation in this nonlinear line defect PCW and those allowing frequencies in Fig. 2.3 are the light that we can used in transmission.

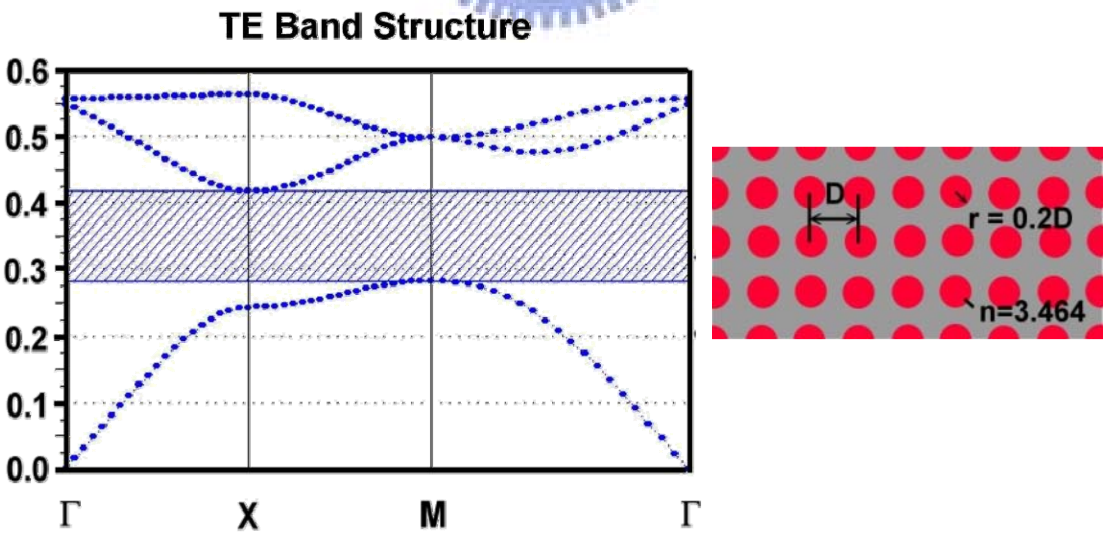

Fig. 2.2 the bandgap of perfect photonic structure.

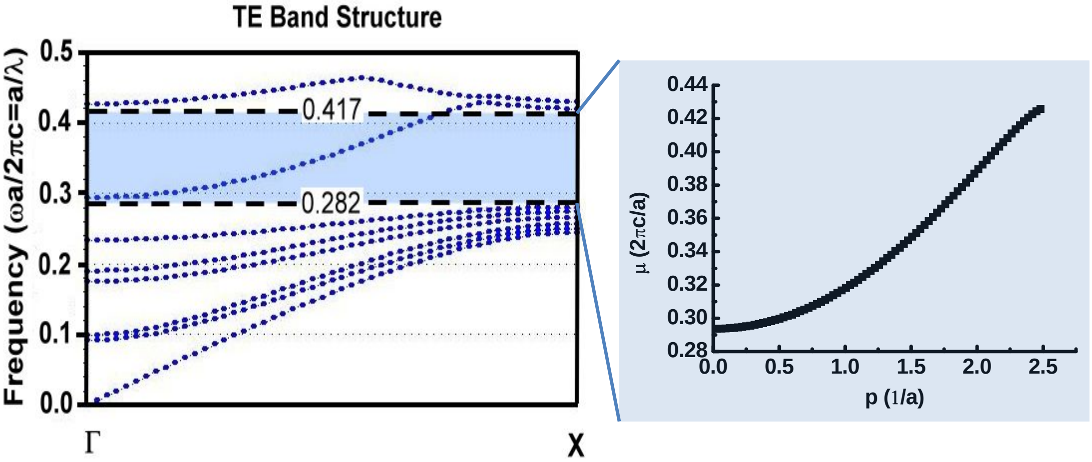

Fig. 2.3 The allowed frequencies in nonlinear line defect PCW and their dispersion relation.

2.4 Discrete soliton– extended nonlinear Schrödinger equation

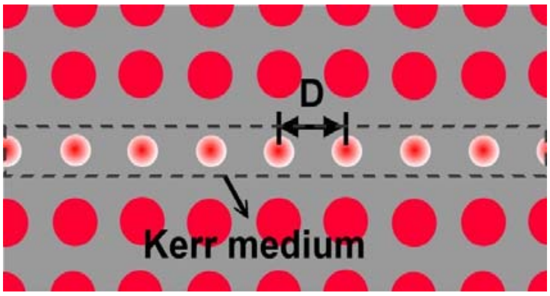

Fig. 2.4 photonic crystal structure with nonlinear defects.

We begin our analysis by considering a periodic sequence of identical coupled defects, similar to that shown schematically in Fig. 2.4. In principle, these defects can confine light in either two- or three-dimensional geometries, provided that they are surrounded by an appropriate photonic bandgap structure. The distance between successive defect points (or primitive cells) is D, and the material is taken here to be Kerr nonlinear. Furthermore, we assume that each defect is single mode, oscillating at an eigenfrequency ω_0. The electromagnetic mode of each defect point in isolation is given by $E = E_0(r)exp(-i\omega_0 t)$ and $H = H_0(r)exp(-i\omega_0 t)$, where $E_0(r)$ and $H_0(r)$ represent the cavity eigenmodes. Evidently, because of proximity, finite coupling exists between successive defects. To describe this coupling process as well as the effects arising from nonlinearity, we derive the nonlinear equations of motion, using the Lorentz reciprocity theorem. To do so, let us assume that the presence of the other cavities near a particular site perturbs the total permittivity from ε to ε'. In general, the perturbed fields $E' = E_0'(r,t)\, exp(-i\omega_0 t)$ and $H' = H_0'(r,t)\, exp(-i\omega_0 t)$ obey $\nabla\times E_0' = \mu_0(i\omega_0 H_0' - \partial H_0'/\partial t)$ and $\nabla\times H_0' = \mu_0(i\omega_0 E_0' - \partial E_0'/\partial t)$. By applying the divergence theorem to the quantity $\nabla\cdot(E_0^{*}\times H_0' + E_0'\times H_0^{*})$, we obtain the Lorentz reciprocity relation:

$$\iiint \nabla\cdot(E_0^{*}\times H_0' + E_0'\times H_0^{*})d\upsilon = \oiint ds\cdot(E_0^{*}\times H_0' + E_0'\times H_0^{*}). \qquad (2.26)$$

Since E_0 and H_0 represent bound modes that vanish at infinity, the surface integral of Eq. (2.26) is equal to zero. Then Eq. (2.26) becomes

$$\iiint d\upsilon[H_0'\cdot(\nabla\times E_0^{*}) - E_0^{*}\cdot(\nabla\times H_0') + H_0^{*}\cdot(\nabla\times E_0') - E_0'\cdot(\nabla\times H_0^{*})] = 0 \qquad (2.27)$$

Substituting Maxwell's equations into Eq. (2.27) and after arranging, it will express as

$$\iiint d\upsilon[i\omega_0(\varepsilon'-\varepsilon)E_0'E_0^{*} - \varepsilon' E_0^{*}\frac{\partial E_0'}{\partial t} - \mu_0 H_0^{*}\frac{\partial H_0'}{\partial t}] = 0. \qquad (2.28)$$

Next, we express the perturbed fields as a time-varying superposition of the bound states, e.g., $E_0'(r,t) = \sum a_m(t)E_{0m}$ and $H_0'(r,t) = \sum a_m(t)H_{0m}$, where the eigenfunctions $E_{0m} = E_0(r - r_m)$ and $H_{0m} = H_0(r - r_m)$ are localized at the lattice points. If, in Eq. (2.28), we let $E_0 = E_{0n}$ and $H_0 = H_{0n}$, and keeping in mind that the material is Kerr nonlinear ($n^2 = n_0^2 + 2n_0 n_2|E|^2$). According to above assumptions, we can obtain the discrete nonlinear evolution equation by Eq. (2.28):

$$i\frac{da_n}{dt} + \sum c_{mn}a_m + \gamma|a_n|^2 a_n = 0, \qquad (2.29)$$

where the linear coupling coefficients c_{mn} are

$$c_{mn} = \frac{\omega_0 \iiint d\upsilon(\varepsilon' - \varepsilon) E_{0n}^{*} \cdot E_{0m}}{\iiint d\upsilon(\mu_0 |H_{0n}|^2 + \varepsilon |E_{0n}|^2)}, \tag{2.30}$$

and the self-phase modulation strength, γ, is given by

$$\gamma = \frac{\alpha \varepsilon_0 \omega_0 \iiint d\upsilon |E_{0n}|^4}{\iiint d\upsilon(\mu_0 |H_{0n}|^2 + \varepsilon |E_{0n}|^2)} \tag{2.31}$$

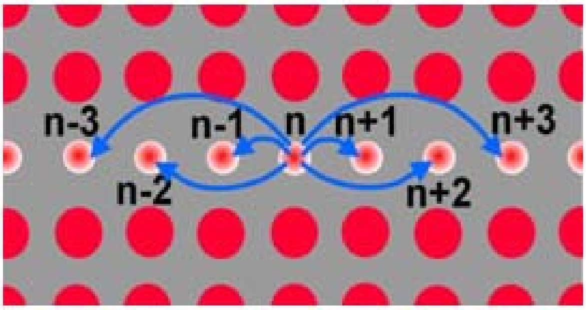

Fig. 2.5 square-array PCW.

We explore the properties of a PCW via the coupling of point defects under the tight-binding approximation, which assumes that the field distribution (or wave function) of PCW is localized at defects. The localized-field couplings up to the third nearest-neighboring (NN) (see Fig. 2.5) are considered to fulfill the dispersion curve [15], and Eq. (2.29) takes the form

$$i\frac{da_n}{dt} + \Delta\omega a_n + c_1(a_{n+1} + a_{n-1}) + c_2(a_{n+2} + a_{n-2}) + c_3(a_{n+3} + a_{n-3}) + \gamma |a_n|^2 a_n = 0 \tag{2.32}$$

$\Delta\omega = c_{mm}$ represents a small shift in the eigenfrequency ω_0 that arises from the presence of neighboring cavities. As a result, the effective eigenfrequency of each resonator in this chain is $\omega_0' = \omega_0 - \Delta\omega$. In addition, $c_1=\pi/2\tau_{c1}$, $c_2=\pi/2\tau_{c2}$, and $c_3=\pi/2\tau_{c3}$ (in inverse time units) are the coupling strength between successive sites, where τ_c is the time required for one cavity to completely couple its energy to its neighbors (in the linear regime). Equation (2.32) describes the evolution dynamics of the optical field in a nonlinear chain of defect points. The equation has the form of a discrete nonlinear Schrödinger equation that is known to exhibit modulation instability and discrete soliton (DS) solutions. Therefore, we call the new discrete nonlinear Schrödinger equation as extended nonlinear Schrödinger equation in the following descriptions.

2.5 Dispersion relation by extended nonlinear Schrödinger equation

In this section we consider the extended NLSE, describing the propagation of a CW beam in a square-array photonic crystal waveguide, and show that this equation exhibits an instability. If we neglect the nonlinear term in Eq.(2.32) temporarily, we can use Eq.(2.32) to fit the curve of dispersion relation in Fig. 2.6 precisely and the fitting coefficients in this curve are $c_1= -0.245547$, $c_2=0.02972$, and $c_3= -0.0027646$. According to this dispersion relation, the inflected point, $p=0.63\pi$, separates the curve into two area, dispersion $\beta_2 > 0$ and dispersion $\beta_2 < 0$. In order to compensate the dispersion, the nonlinear factor will be negative ($\gamma < 0$) if $\beta_2 > 0$ and vice versa.

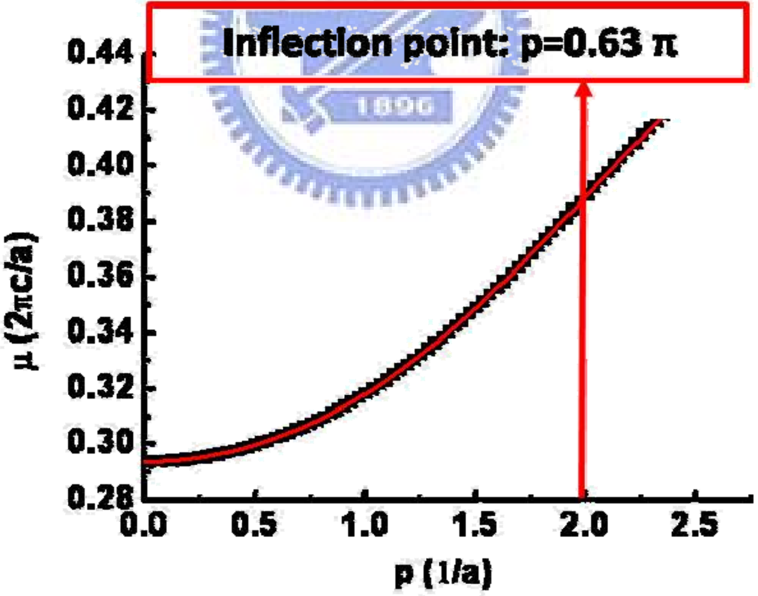

Fig. 2.6 The dispersion relation fitting. The red line represents the fitting curve and the black points indicate the actual values.

2.6 Modulation instability– extended nonlinear Schrödinger equation

After knowing the sign of nonlinear coefficient (γ) in different wave vectors (p) that correspond to the dispersion relation, now, we begin our analysis of modulation instability. First, we assume the perturbed CW field distribution of Eq. (2.32) as

$$a_n = [\phi_0 + u(t)e^{iqn} + v^*(t)e^{-iqn}]e^{i(pn-\frac{\mu}{\hbar}t)}, \tag{2.33}$$

where ϕ_0 is the amplitude of the eigenmode prior to the nonlinear perturbation, $u(t)$ and $v^*(t)$ represent small perturbations from other guiding modes with propagation wavevector $p+q$ and $p-q$ or with the perturbation wavevectors q and - q. Substituting the perturbed CW field into Eq. (2.32) and linearizing the equation, we obtain coupled linear equations of the system

$$\begin{aligned} &\left.\begin{cases} \left[\mu+\Delta\omega+2c_1\cos(p+q)+2c_2\cos(2p+2q)+2c_3\cos(2p+2q)\right]u(t) \\ +2\gamma\left|\phi_0\right|^2 u(t)-\gamma\left|\phi_0\right|^2 v(t) \end{cases}\right\} = -iu'(t) \\ &\left.\begin{cases} \left[\mu+\Delta\omega+2c_1\cos(p-q)+2c_2\cos(2p-2q)+2c_3\cos(2p-2q)\right]u(t) \\ +2\gamma\left|\phi_0\right|^2 v(t)-\gamma\left|\phi_0\right|^2 u(t) \end{cases}\right\} = -iv'(t) \end{aligned} \tag{2.33}$$

with $\mu(p) = -\Delta\omega - 2c_1\cos(p) - 2c_2\cos(2p) - 2c_3\cos(3p) + \gamma\left|\phi_0\right|^2$.

Solving Eq. (2.33), we have the dispersion relation:

$$\omega(p,q) = \frac{1}{2}[-(A+B) \pm \sqrt{(A+B)(A+B-4\gamma\,|\,\phi_0\,|^2)}], \tag{2.34}$$

where $A+B = -8[c_1\cos(p)\sin^2(\frac{q}{2}) + c_2\cos(2p)\sin^2(q) + c_3\cos(3p)\sin^2(\frac{3q}{2})]$. (2.35)

The dispersion relation $\omega(p, q)$ is imaginary and the CW becomes unstable, when $(A+B)(A+B - 4\gamma|\phi_0|^2) < 0$. This is the so-called modulation instability [17], which is closely connected with the occurring of solitary-wave solutions of NLSE. The MI growth rate g, also called the MI gain, is related to the imaginary part of ω, i.e.,

$$\mathrm{Im}(\omega(p, q)) = \frac{1}{2}\left|(A+B)(A+B-4\gamma|\phi_0|^2)\right|^{\frac{1}{2}} . \tag{2.36}$$

2.7 Fourth-order Runge-Kutta method for solving extended NLSE

Problems involving ordinary differential equations (ODEs) can always be reduced to the study of sets of first-order differential equations. For example the second-order equation

$$\frac{d^2y}{dx^2}+q(x)\frac{dy}{dx}=r(x) \tag{2.37}$$

can be rewritten as two first-order equations

$$\frac{dy}{dx}=z(x),$$

$$\frac{dz}{dx}=r(x)-q(x)z(x), \tag{2.38}$$

where z is a new variable. This exemplifies the procedure for an arbitrary ODE. The usual choice for the new variables is to let them be just derivatives of each other (and of the original variable). Occasionally, it is useful to incorporate into their definition some other factors in the equation, or some powers of the independent variable, for the purpose of mitigating singular behavior that could result in overflows or increased round off error. Let common sense be your guide: If you find that the original variables are smooth in a solution, while your auxiliary variables are doing crazy things, then figure out why and choose different auxiliary variables. The generic problem in ordinary differential equations is thus reduced to the study of a set of N coupled *first-order* differential equations for the functions y_i, $i = 1, 2, \ldots, N$, having the general form

$$\frac{dy_i(x)}{dx} = f_i(x, y_1, \ldots, y_N), \quad i=1,2,\ldots,N, \tag{2.39}$$

where the functions fi on the right-hand side are known. A problem involving ODEs is not completely specified by its equations. Even more crucial in determining how to attack the problem numerically is the nature of the problem's boundary conditions. Boundary conditions are algebraic conditions on the values of the functions y_i in Eq. (3). In general they can be satisfied at discrete specified points, but do not hold between those points, i.e., are not preserved automatically by the differential equations. Boundary conditions can be as simple as requiring that certain variables have certain numerical values, or as complicated as a set of nonlinear algebraic equations among the variables. Usually, it is the nature of the boundary conditions that determines which numerical methods will be feasible. Boundary conditions divide into two broad categories.

1. In *initial value problems* all the y_i are given at some starting value x_s, and it is desired to find the y_i's at some final point x_f, or at some discrete list of points (for example, at tabulated intervals).
2. In *two-point boundary value problems*, on the other hand, boundary conditions are specified at more than one x. Typically, some of the conditions will be specified at x_s and the remainder at x_f.

This thesis will consider exclusively the initial value problem, deferring two point boundary value problems. The underlying idea of any routine for solving the initial value problem is always this: Rewrite the dy's and dx's in Eq. (3) as finite steps Δy and Δx, and multiply the equations by Δx. This gives algebraic formulas for the change in the functions when the independent variable x is "stepped" by one "step size" Δx. In the limit of making the step size very small, a good approximation to the underlying differential equation is achieved. Literal implementation of this procedure results in *Euler's method* (Eq. (4), below), which is, however, not recommended for any practical use. Euler's method is conceptually important, however; one way or another, practical methods all come down to this same idea: Add small increments to your functions corresponding to derivatives (right-hand sides of the equations) multiplied by step sizes. In this thesis we consider *Runge-Kutta* methods for solving initial value problems for ODEs. The methods propagate a solution over an interval by combining the information from several Euler-style steps (each involving one evaluation of the right-hand f's), and then using the information obtained to match a Taylor series expansion up to some higher order. However, Runge-Kutta is what you use when (i) you don't know any better, or (ii) you have an intransigent problem where Bulirsch-Stoer is failing, or (iii) you have a trivial problem where computational efficiency is of no concern. Runge-Kutta succeeds virtually always; but it is not usually fastest, except when evaluating f_i is cheap and moderate accuracy ($\leq 10^{-5}$) is required.

Now, we introduce this method more explicitly. The formula for the Euler method is

$$y_{n+1} = y_n + hf(x_n, y_n), \tag{2.40}$$

which advances a solution from *xn* to $x_{n+1} \equiv x_{n+h}$. The formula is unsymmetrical: It advances the solution through an interval *h*, but uses derivative information only at the beginning of that interval (see Fig. 2.7). That means (and you can verify by expansion in power series) that the step's error is only one power of *h* smaller than the correction, i.e., $O(h^2)$ added to Eq. (4). There are several reasons that Euler's method is not recommended for practical use, among them, (i) the method is not very accurate when compared to other, fancier, methods run at the equivalent step size, and (ii) neither is it very stable.

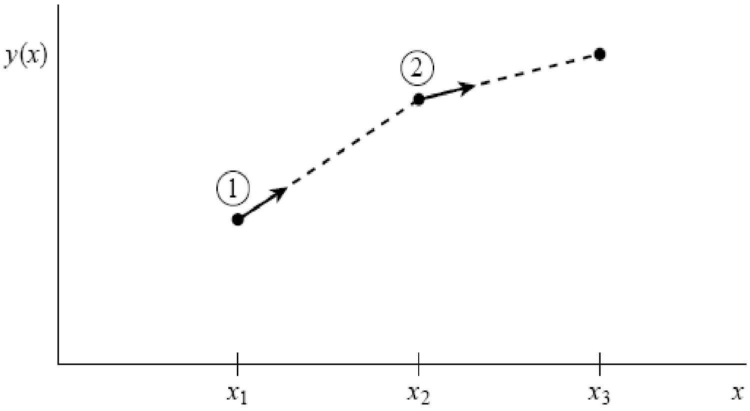

Fig. 2.7 Euler's method. In this simplest (and least accurate) method for integrating an ODE, the derivative at the starting point of each interval is extrapolated to find the next function value. The method has first-order accuracy.

Consider, however, the use of a step like Eq. (4) to take a “trial” step to the midpoint of the interval. Then use the value of both x and y at that midpoint to compute the “real” step across the whole interval. Figure 2.8 illustrates the idea. In equations,

$$k_1 = hf(x_n, y_n)$$

$$k_2 = hf(x_n + \frac{1}{2}h, y_n + \frac{1}{2}k_1)$$

$$y_{n+1} = y_n + k_2 + O(h^3), \qquad (2.41)$$

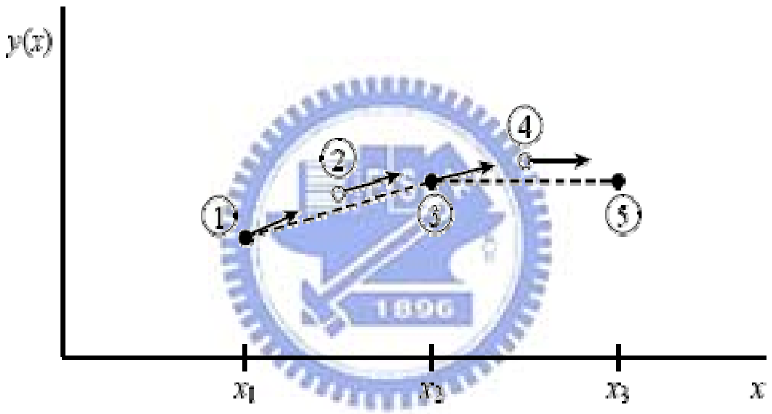

Fig. 2.8 Midpoint method. Second-order accuracy is obtained by using the initial derivative at each step to find a point halfway across the interval, then using the midpoint derivative across the full width of the interval. In the figure, filled dots represent final function values, while open dots represent function values that are discarded once their derivatives have been calculated and used.

As indicated in the error term, this symmetrization cancels out the first-order error term, making the method *second order*. [A method is conventionally called *n*th order if its error term is $O(h^{n+1})$.] In fact, Eq. (5) is called the *second-order Runge-Kutta* or *midpoint* method.

We needn't stop there. There are many ways to evaluate the right-hand side $f(x, y)$ that all agree to the first order, but that have different coefficients of higher-order error terms. Adding up the right combination of these, we can eliminate the error terms order by order. That is the basic idea of the Runge-Kutta method [41]. Abramowitz and Stegun, and Gear, give various specific formulas that derive from this basic idea. By far the most often used is the classical *fourth-order Runge-Kutta formula*, which has a certain sleekness of organization about it:

$$k_1 = hf(x_n, y_n)$$

$$k_2 = hf(x_n + \frac{1}{2}h, y_n + \frac{1}{2}k_1)$$

$$k_3 = hf(x_n + \frac{1}{2}h, y_n + \frac{1}{2}k_2)$$

$$k_4 = hf(x_n + h, y_n + k_3)$$

$$y_{n+1} = y_n + \frac{k_1}{6} + \frac{k_2}{3} + \frac{k_3}{3} + \frac{k_4}{6} + O(h^5) \tag{2.42}$$

The fourth-order Runge-Kutta method requires four evaluations of the right-hand side per step *h* (see Fig. 2.9). This will be superior to the midpoint method Eq. (5) if at least twice as large a step is possible with Eq. (6) for the same accuracy. Is that so?

The answer is: often, perhaps even usually, but surely not always! This takes us back to a central theme, namely that *high order* does not always mean *high accuracy*. The statement "fourth-order Runge-Kutta is generally superior to second-order" is a true one, but you should recognize it as a statement about the contemporary practice of science rather than as a statement about strict mathematics. That is, it reflects the nature of the problems that contemporary scientists like to solve.

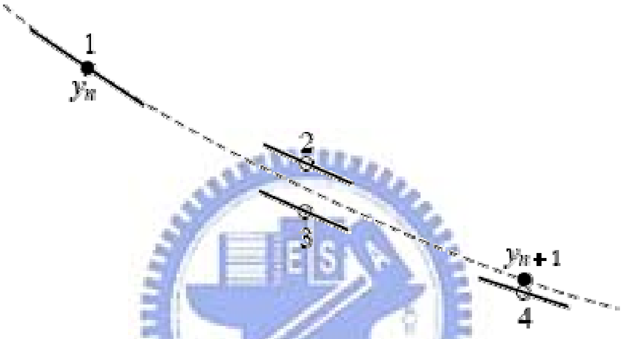

Fig. 2.9 Fourth-order Runge-Kutta method. In each step the derivative is evaluated four times: once at the initial point, twice at trial midpoints, and once at a trial endpoint. From these derivatives the final function value (shown as a filled dot) is calculated.

Chapter 3 Results and Discussion

3.1 Results of analytic solution

According to the condition of MI, $(A+B)(A+B - 4\gamma|\phi_0|^2) < 0$, we know if $\gamma < 0$ (defocusing nonlinearity), $(A+B) < 0$ and $(A+B - 4\gamma|\phi_0|^2) > 0$ will be established, and the MI gain occurs in the area Ⅰ of Fig. 3.1. If $\gamma > 0$ (focusing nonlinearity), the situation will be reversed and the MI gain occurs in the area Ⅱ of Fig. 3.1. The MI gain can be acquired immediately from Fig. 3.1 as $\sqrt{\alpha\beta}$, where the magnitudes α and β represent the values of $|A+B|$ and $|(A+B-4\gamma|\phi_0|^2)|$.

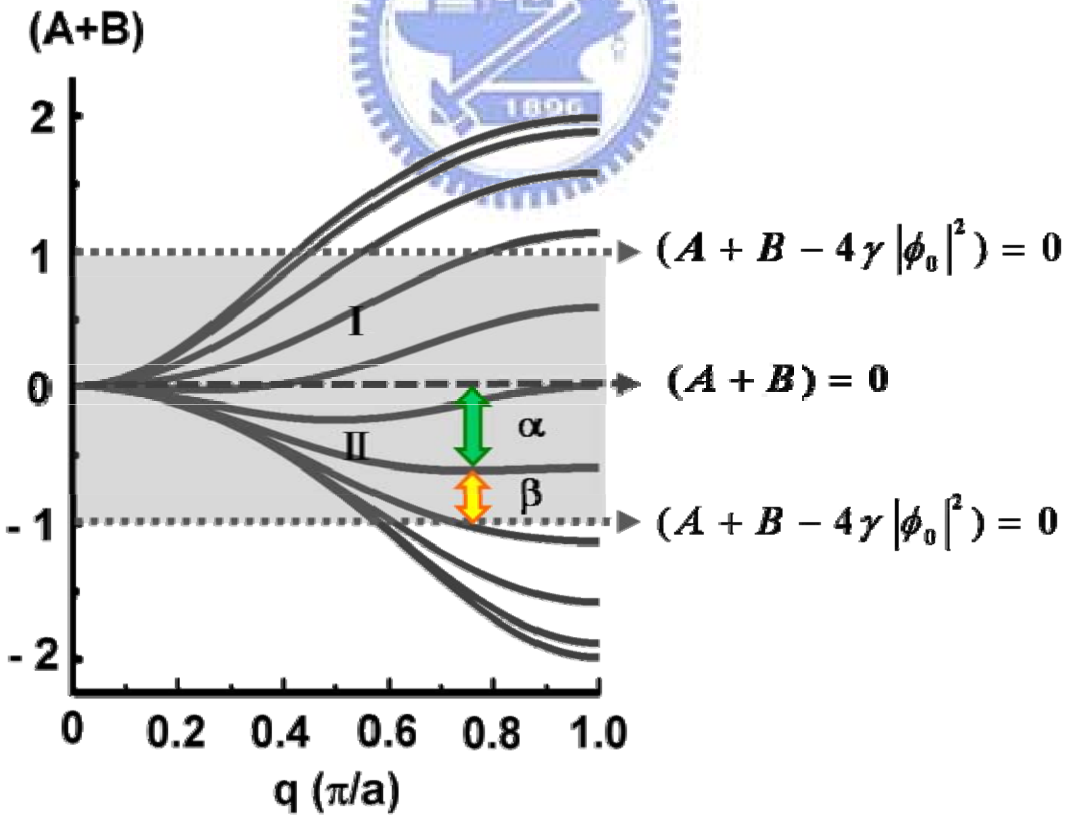

Fig. 3.1 (A+B) versus q for square-array PCW considering coupling up to the third NN.

After knowing how to find the condition of modulation instability and to calculate the value of MI gain by Fig. 3.1, we want to probe for the MI gain profile in different γ, p, and q. Figures 3.2 and 3.3 represent the relationship between MI gain and different p and q with γ = - 0.005 and γ = 0.005 in the square-array PCW. We can find a big different between Fig. 3.2 and Fig. 3.4. Considering some specific p, if γ = - 0.005 < 0, there are two regions of q having MI gain with the same p, but only one MI gain region when γ = 0.005 > 0. Additionally, we also want to compare the above phenomenon obtained with the condition of the MI gain that only considering the nearest-neighboring coupling. The results obtained only considering the nearest-neighboring coupling as shown in Fig. 3.4 and Fig. 3.5, which can not completely describe the dispersion curve of PCW, predict a single MI gain region occurring no matter γ is positive or negative.

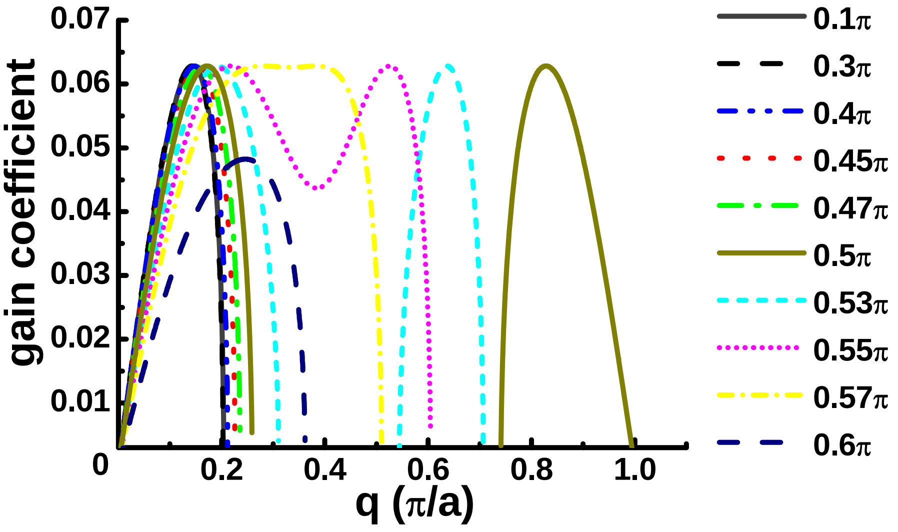

Fig. 3.2 MI gain profile (γ = - 0.005 < 0) in the square-array PCW.

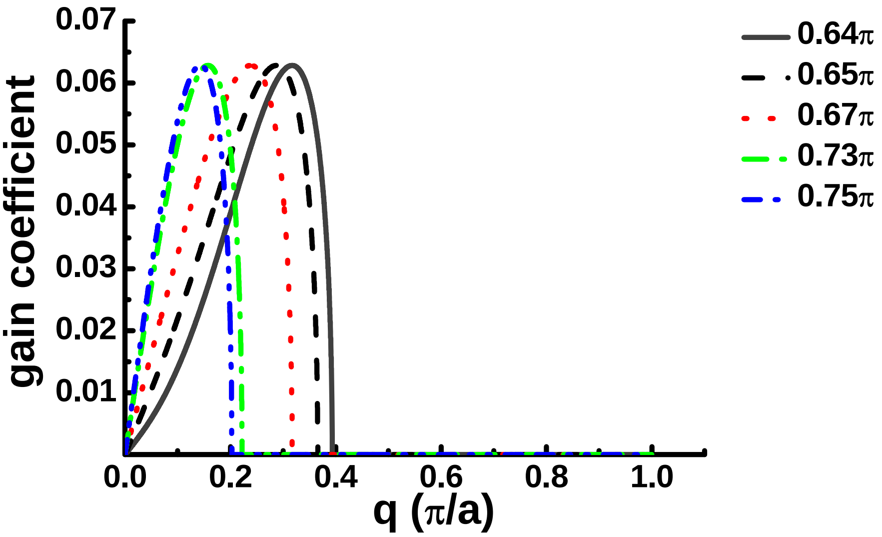

Fig. 3.3 MI gain profile ($\gamma = 0.005 > 0$) in the square-array PCW.

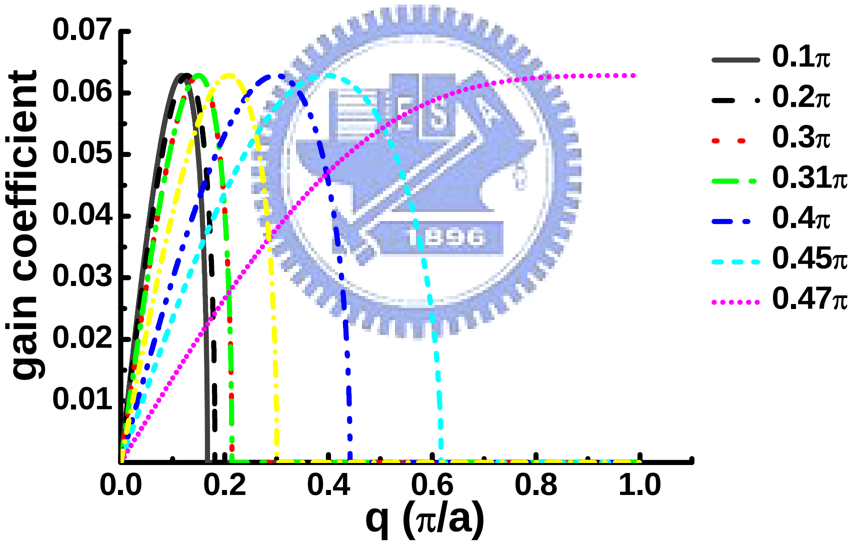

Fig. 3.4 MI gain profile for $\gamma < 0$ in square-array PCW only considering coupling of the NN defects.

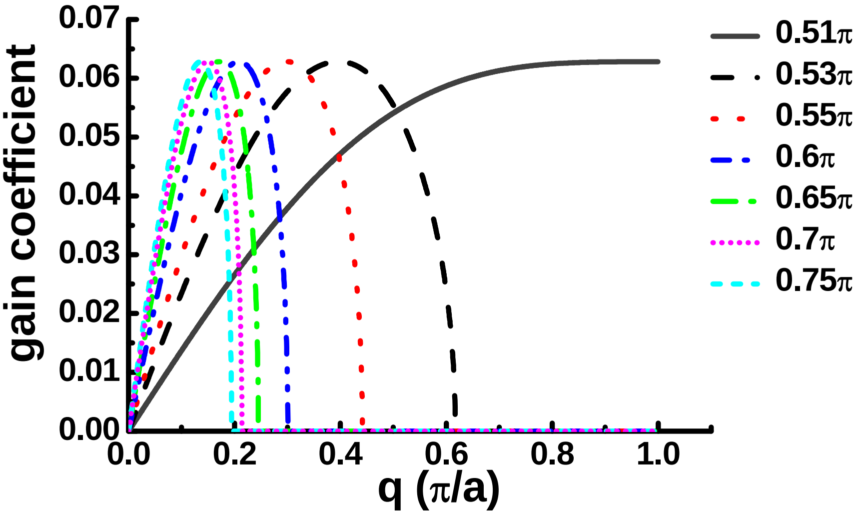

Fig. 3.5 MI gain profile for $\gamma > 0$ in square-array PCW only considering coupling of the NN defects.

Because learning of the special case in the square-array PCW, we try to analyze the MI gain with the condition of $\gamma = -0.005 < 0$. The two MI gain regions exist because of considering beyond the NN defects coupling. In other words, if only considering NN defect coupling, we can't find MI gain in the same p distributed into two scopes in the gain profile. We give an example of $p = 0.49\pi$ which has two regions of q having MI gains. Figure 3.6 is a chart of the MI gain, (A+B), and $(|(A+B-4\gamma|\phi_0|^2)|)$. We can see the curves that consider up to the 2nd order and the 3rd order NN defect are almost overlap, so we just compare the formulas included c_1 with the formulas included c_1 and c_2 in the following discussion. Seeing Eq. (2.4), if p has been given a constant value, the term of cos(p) will also become a constant and the quantities of MI gain will be decided by the values of q only. There are two terms included q in Eq. (2.4), namely, $-8c_1^* \cos(0.49\pi)\sin^2(q/2)$ and $-8c_2^* \cos(0.98\pi)\sin^2(q)$. We analyze the profiles with only considering the NN defect firstly and when the values of q increase from 0 to $\pi/2$, the values of the first term, $-8c_1^* \cos(0.49\pi)\sin^2(q/2)$, decrease from 0 to -0.0616. Therefore, the values of (A+B) is all negatives and after plus a positive value, $-4\gamma|\phi_0|^2$ ($\gamma < 0$), the values of $(|(A+B-4\gamma|\phi_0|^2)|)$ are all positive (see Fig. 3.6). Next, we consider the coupling up to the 2nd order defects. The first term in Eq. (2.4) decreases from 0 to -0.2375 then increases from -0.2375 to 0, as q varies from 0, $\pi/2$ then to π. For this reason, we can get the values of $(|(A+B-4\gamma|\phi_0|^2)|)$ in area I and area Ⅱ are still positive but others become negatives (see Fig. 3.6). We call this phenomenon “gain suppression”. This is a remarkable difference if we consider the effect beyond the NN defect so considering the coupling beyond the nearest-neighboring defects is essential.

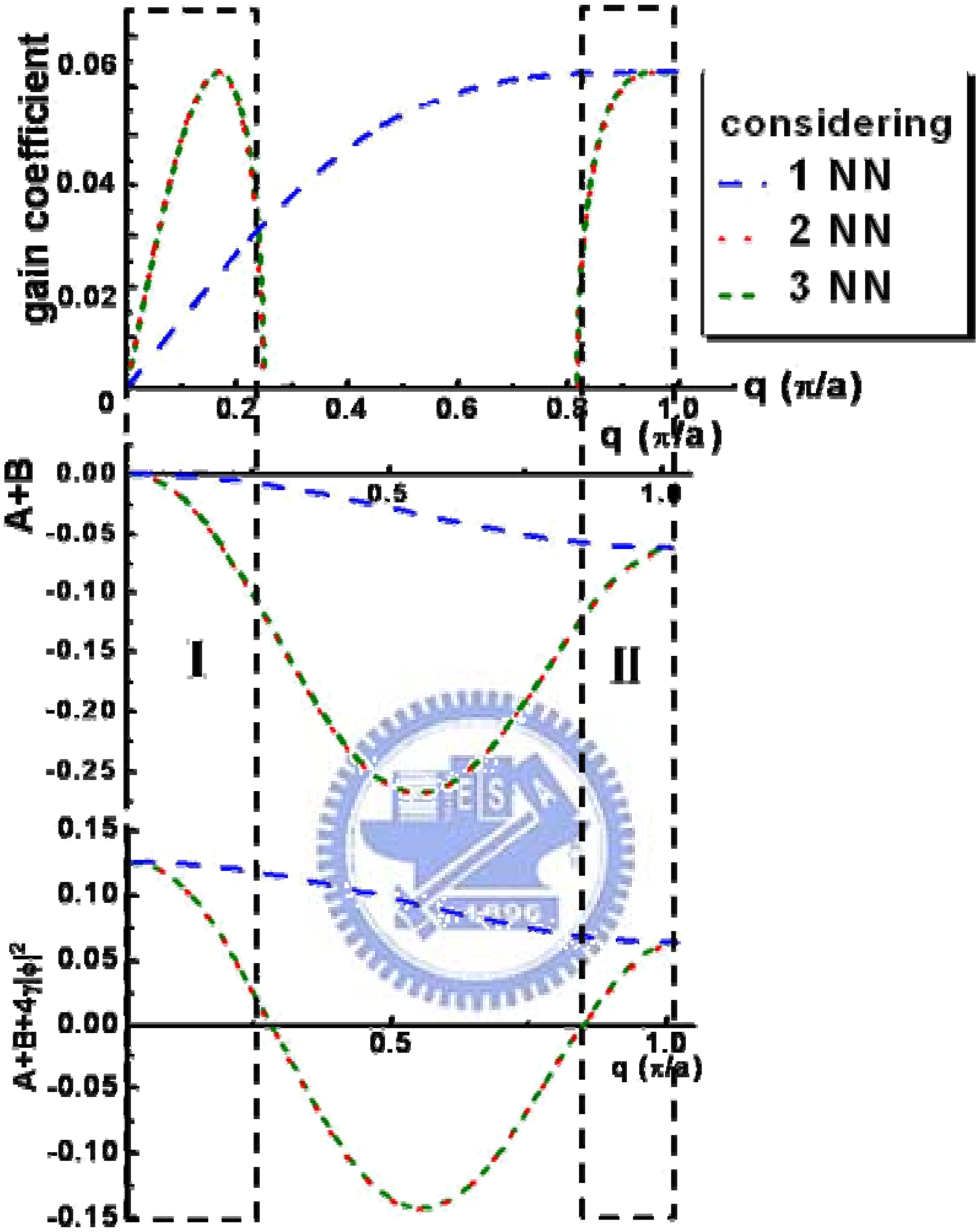

Fig. 3.6 With p=0.49π, the green lines represent the case of considering beyond the NN defect effect and the red ones stand for the case of considering only NN defect effect. The upper picture is the MI gain distribution. The middle one tells us the values of (A+B+4F). The bottom profile represents the variation of (A+B).

In order to discuss the MI gain profile in Fig. 3.7, we follow with interest where the maximum (g_{max}) in the MI gain profile first. We set the differentiation of MI gain to zero and obtain two conditions: (A) $A+B-2\gamma|\phi_0|^2=0$ and (B) $\frac{d}{dq}(A+B)=0$. Under $\gamma = -0.005 < 0$ the MI gain profile in Fig. 3.7 has two g_{max} for some given p's if we consider the coupling up to the third nearest-neighboring (NN) coupling. In the square-array PCW, it occurs when $0.49\,\pi \le p \le 0.57\,\pi$ and these two gain maxima are determined by condition (A). Since $p > 0.57\,\pi$, the outcome of MI gains return to one g_{max}, but these values are smaller than the magnitudes in the condition of $p \le 0.57\pi$ and they decrease with the increasing p. On the other hand, the condition (B) should be considered if condition (A) can't apply, such as the case of $p = 0.6\pi$. Moreover, g_{max} satisfied by condition (B) is less than that by condition (A).

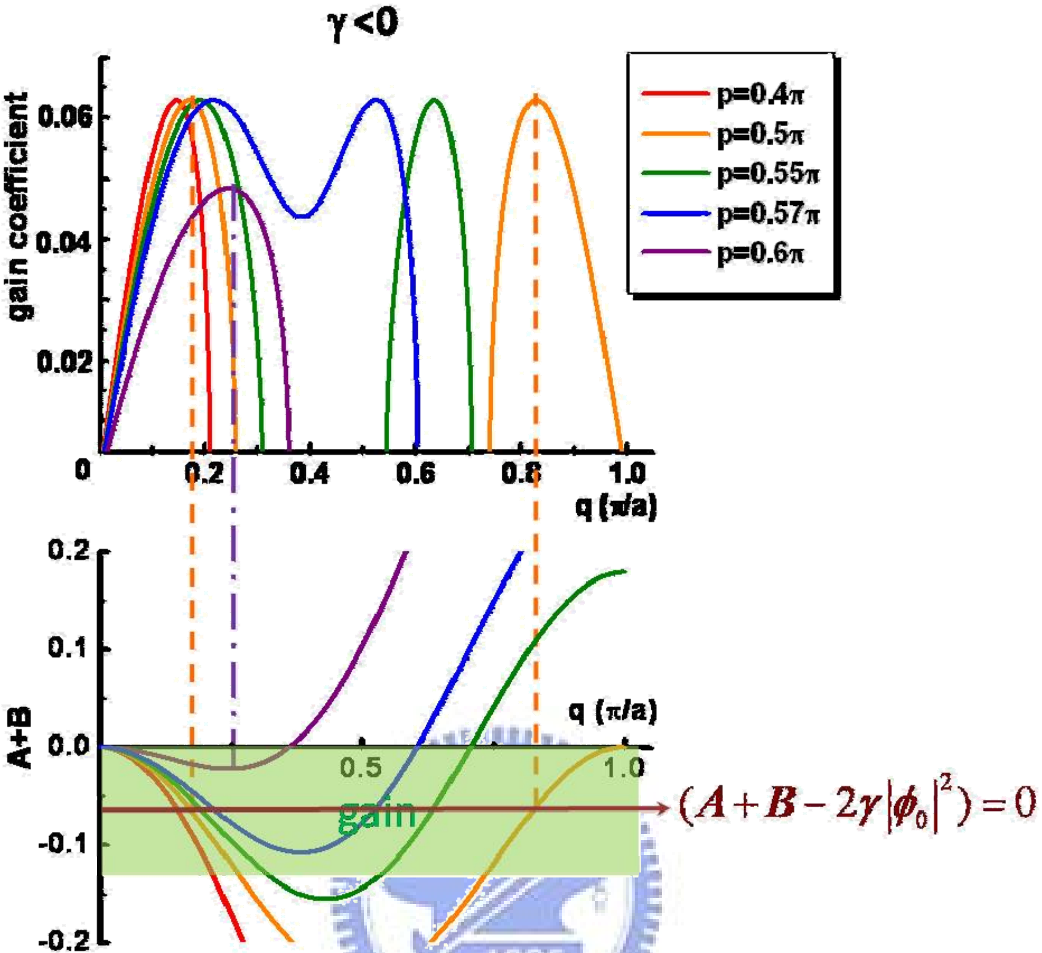

Fig. 3.7 MI gain profile for γ < 0 in square-array PCW considering coupling up to the third NN defects.

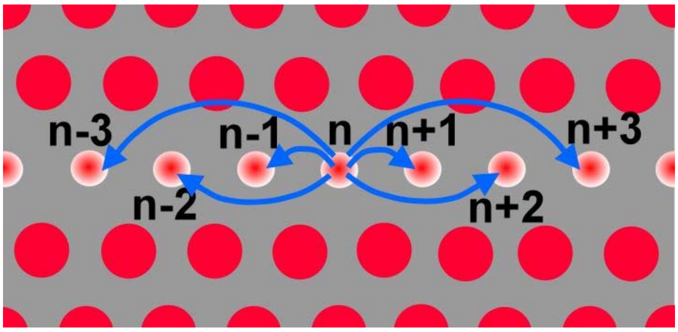

Fig. 3.8 triangular-array PCW.

After discussing the modulation instability gain in square-array PCW, now, we want to discuss the MI gain in triangular-array PCW (see Fig. 3.8) and make a comparison between these two different PCW structures. We use the same method to comprehend the MI gain contour in triangular-array PCW.

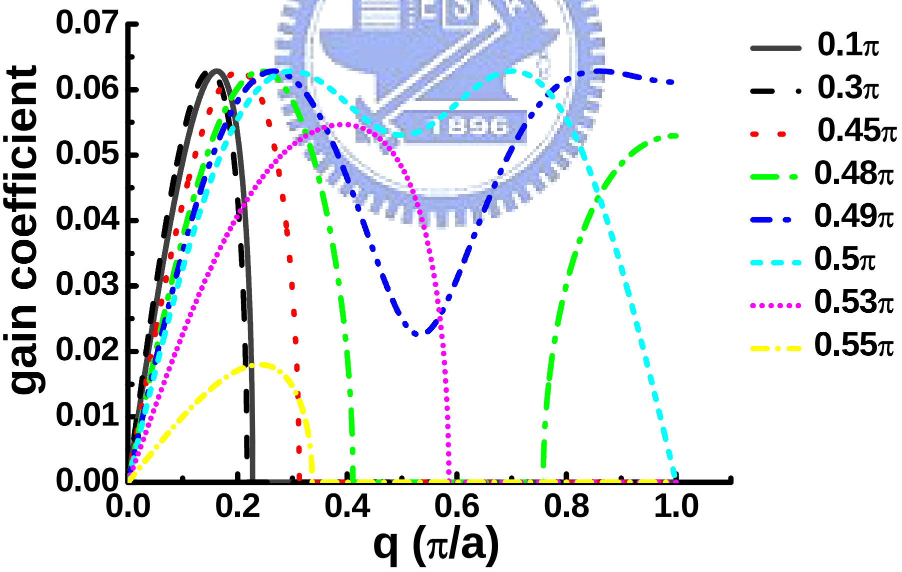

Fig. 3.9 MI gain profile ($\gamma = - 0.005 < 0$) in the triangular-array PCW.

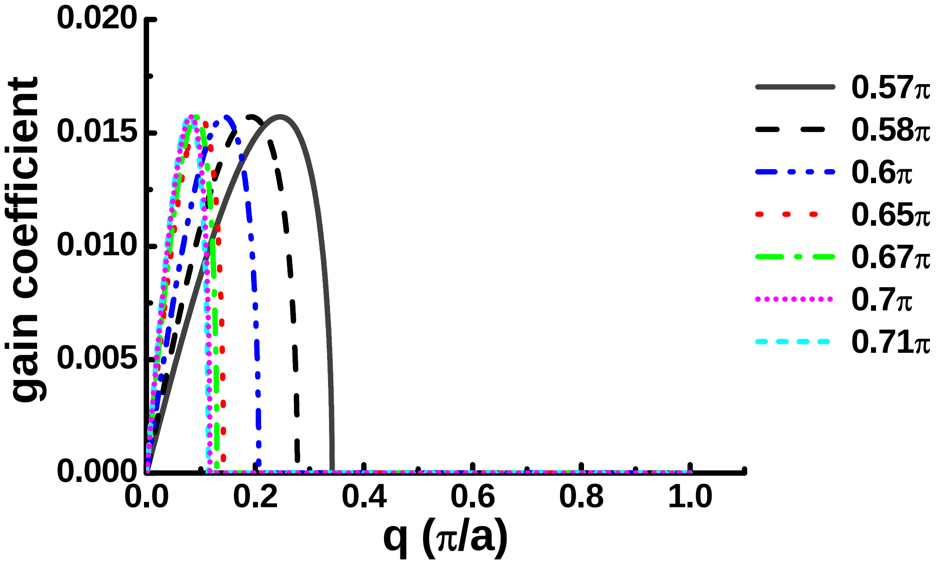

Fig. 3.10 MI gain profile ($\gamma = 0.005 > 0$) in the triangular -array PCW.

From Fig. 3.9, we also can find the two regions having MI gain for some values of p and they exist in $p = 0.48\,\pi$ to $0.51\,\pi$. Therefore, we judge that in the same condition the scope of p which has two g_{max} in square-array PCW is larger than in triangular-array PCW. Furthermore, the result in Fig. 3.10 is the same as Fig. 3.5 in square-array PCW. We only can find one region of MI gain existing for each p with the condition of $\gamma < 0$.

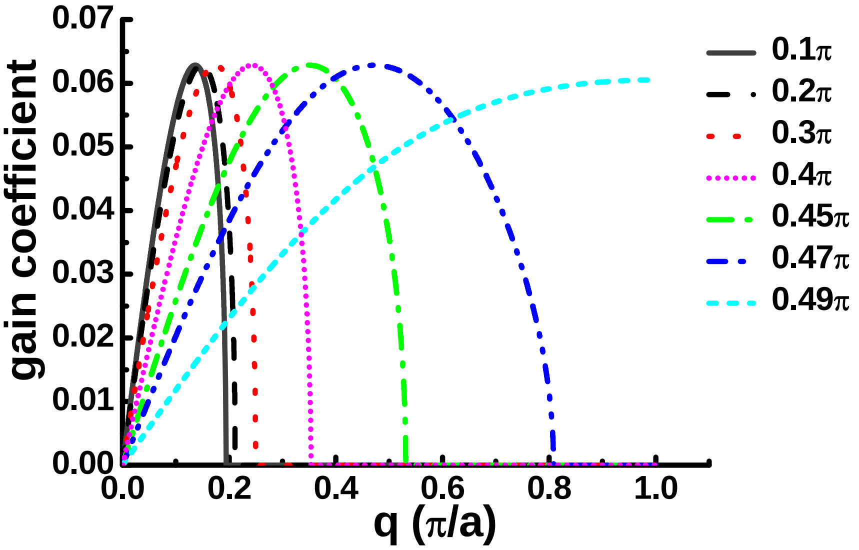

Fig. 3.11 MI gain profile for $\gamma < 0$ in triangular-array PCW only considering coupling of the NN defects.

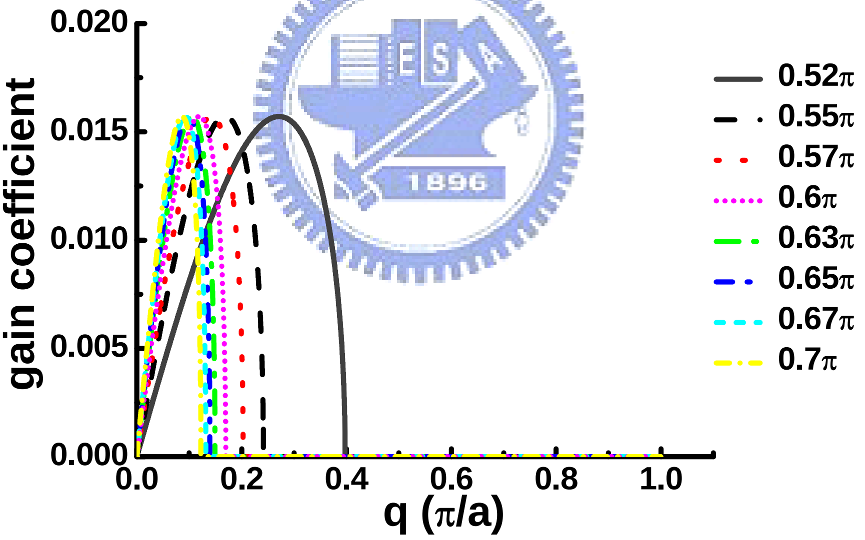

Fig. 3.12 MI gain profile for $\gamma > 0$ in triangular-array PCW only considering coupling of the NN defects.

According to Figs. 3.4, 3.5, 3.11, and 3.12, no matter $\gamma > 0$ or $\gamma < 0$, there is no two g_{max} in both square-array PCW and triangular-array PCW if only the NN defect coupling is considered.

The biggest influence on considering the coupling effect more than the nearest neighbor is shifting the inflected point from 0.5 π to 0.63 π in the dispersion curve and it leads to the MI gain profile has different distribution as the above description. Therefore, it is absolutely essential to consider more than NN coupling in nonlinear PCWs.

3.2 Results of simulation

Although the MI gain has been discussed in dissimilar conditions by analytic solution, we still want to make sure of these results by directly solving the extended NLSE numerically. The fourth order Runge-Kutta method is used to do the simulation. We choose a wave with perturbation to be the light source of input and observe its variation with time in the spatial domain.

Now, we consider the condition of $\gamma = -0.005 < 0$ in square-array PCW and select three different *p,* 0.4π, 0.5π, and 0.6π as examples (see Fig. 3.13). Figure 3.14 shows the initial intensity of electric fields and their spectra after making Fourier transform. The intensities of these three cases are almost the same in space and only distribute in p, p+q, and p-q in spectrum. Moreover, we can see that the intensity is located primarily in p, which is the wave vector with incident plane wave in each case.

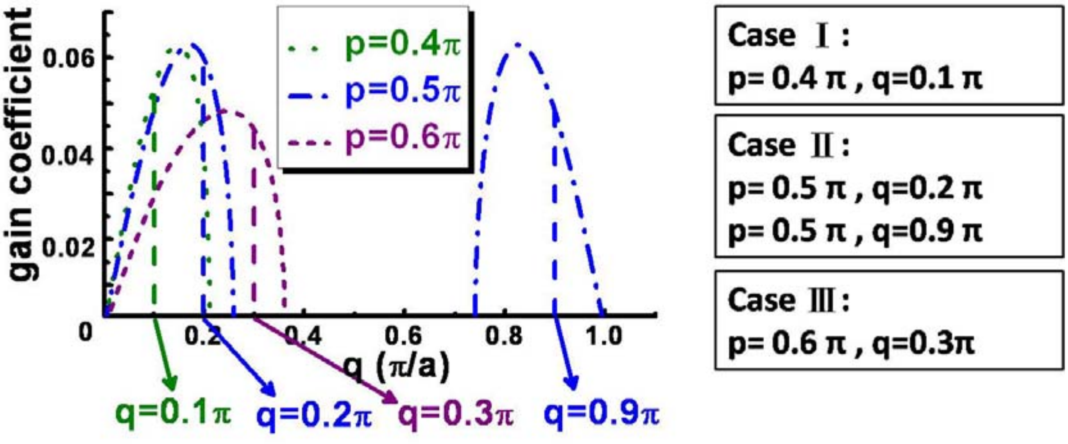

Fig. 3.13 The cases of our simulation.

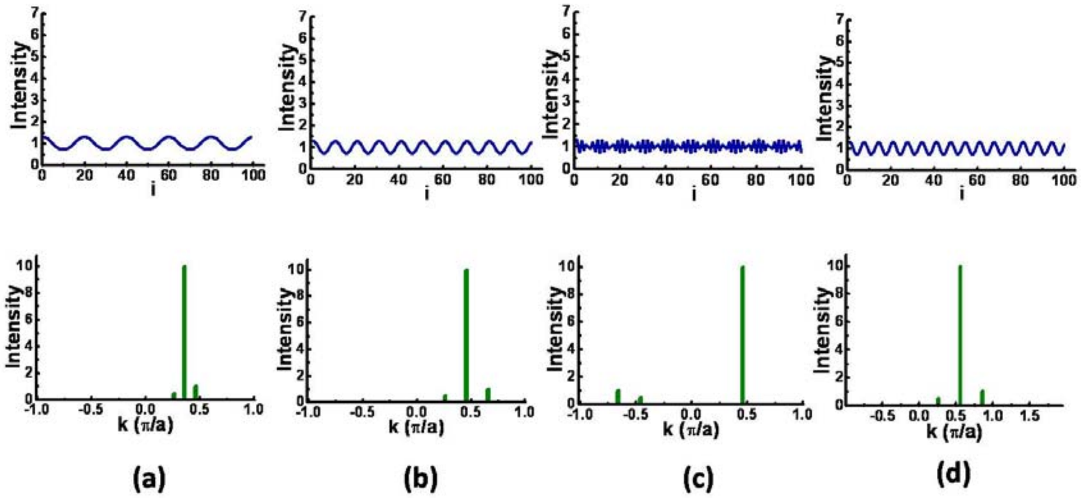

Fig. 3.14 The initial intensity of electric fields in three cases. (a) Case Ⅰ : p=0.4π, q=0.1π; (b) Case Ⅱ : p=0.5π, q=0.2π; (c) Case Ⅱ : p=0.5π, q=0.9π; (d) Case Ⅲ : p=0.6π, q=0.3π

After evolution, the perturbations became unstable and the soliton chains were formed. We can observe that the distribution of intensity is disordered in spectrum and the intensity that locates in p is transferred to other spatial frequencies (see Fig. 3.15). Besides, the MI gain in case Ⅲ is smaller than others so its ability of producing soliton chain is weaker.

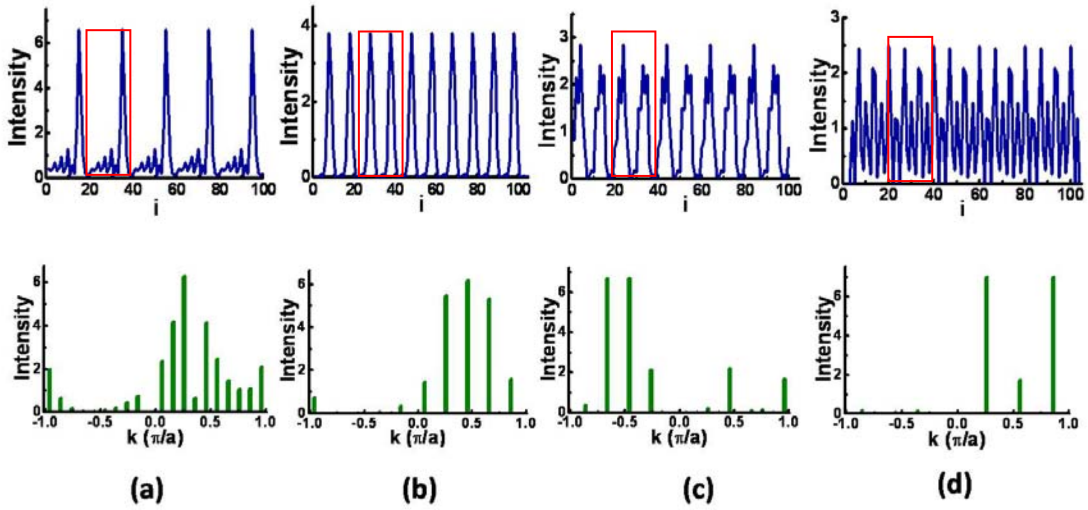

Fig. 3.15 The intensity of electric fields in three cases after evolution. (a) Case Ⅰ : p=0.4π, q=0.1π; (b) Case Ⅱ : p=0.5π, q=0.2π; (c) Case Ⅱ : p=0.5π, q=0.9π; (d) Case Ⅲ : p=0.6π, q=0.3π.

According to these messy spectra, we conjectured that the resultant propagating wave was mixture of spatial temporal solitons with dispersive wave. Therefore, in order to have real and pure solitons, we extracted a period of electric field to be the initial pulse for soliton propagation and tried to separate the soliton and dispersive wave as it propagating along the PCW.

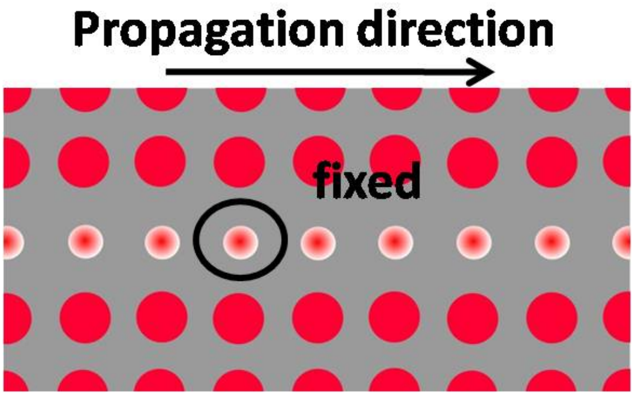

Fig. 3.16 Invariable special domain and variable time domain.

In the above section, we have obtained the gain profile by analytic solution. Now we still want to describe the magnitude of MI gain through simulation. Look at Fig. 3.16, we chose a fixed position and trace variation of electric field following iterations of time steps. During the simulation, we should take care that before the growing pulse begins to separate. The MI gain means the growing rate in the sketch of amplitude. The exponential curve in Fig. 3.17 replaces the increase of amplitude. We can obtain the growing rate of amplitude by taking logarithms of this curve. Therefore, the MI gain can be defined as the slope, Δy/Δx, in Fig. 3.18.

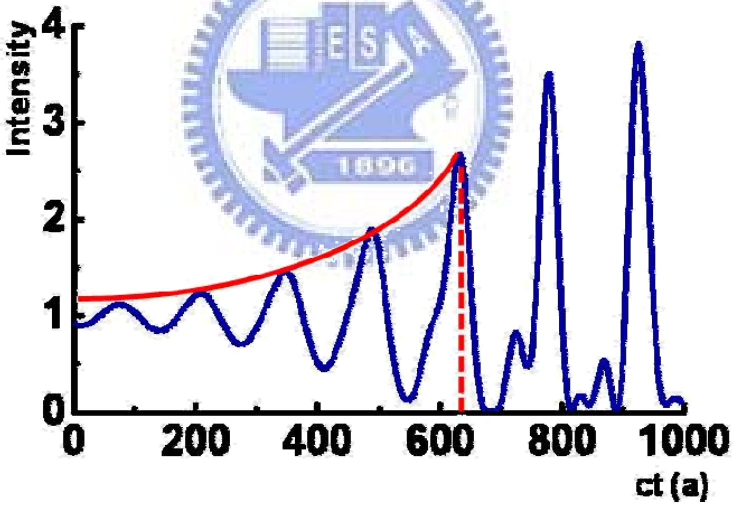

Fig. 3.17 The intensity of electric field in time domain.

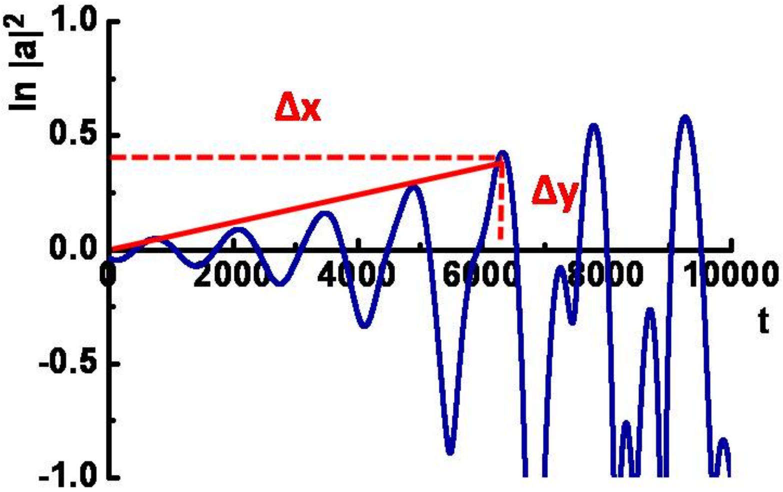

Fig. 3.18 Taking logarithmic scale from Figure 3.17.

After knowing how to find the value of g_{max} by simulation, we tried to reconstruct the MI gain profiles which were produced by analytic solutions. Now, we picked three cases (see Fig. 3.19(a)) to compare the results of these two different methods. In Figs. 3.19(b), (c), and (d), the curves represent the analytic solutions and the dots indicate the results of simulation. By means of these three figures, we knew the results of simulation match quite well with the analytic solutions.

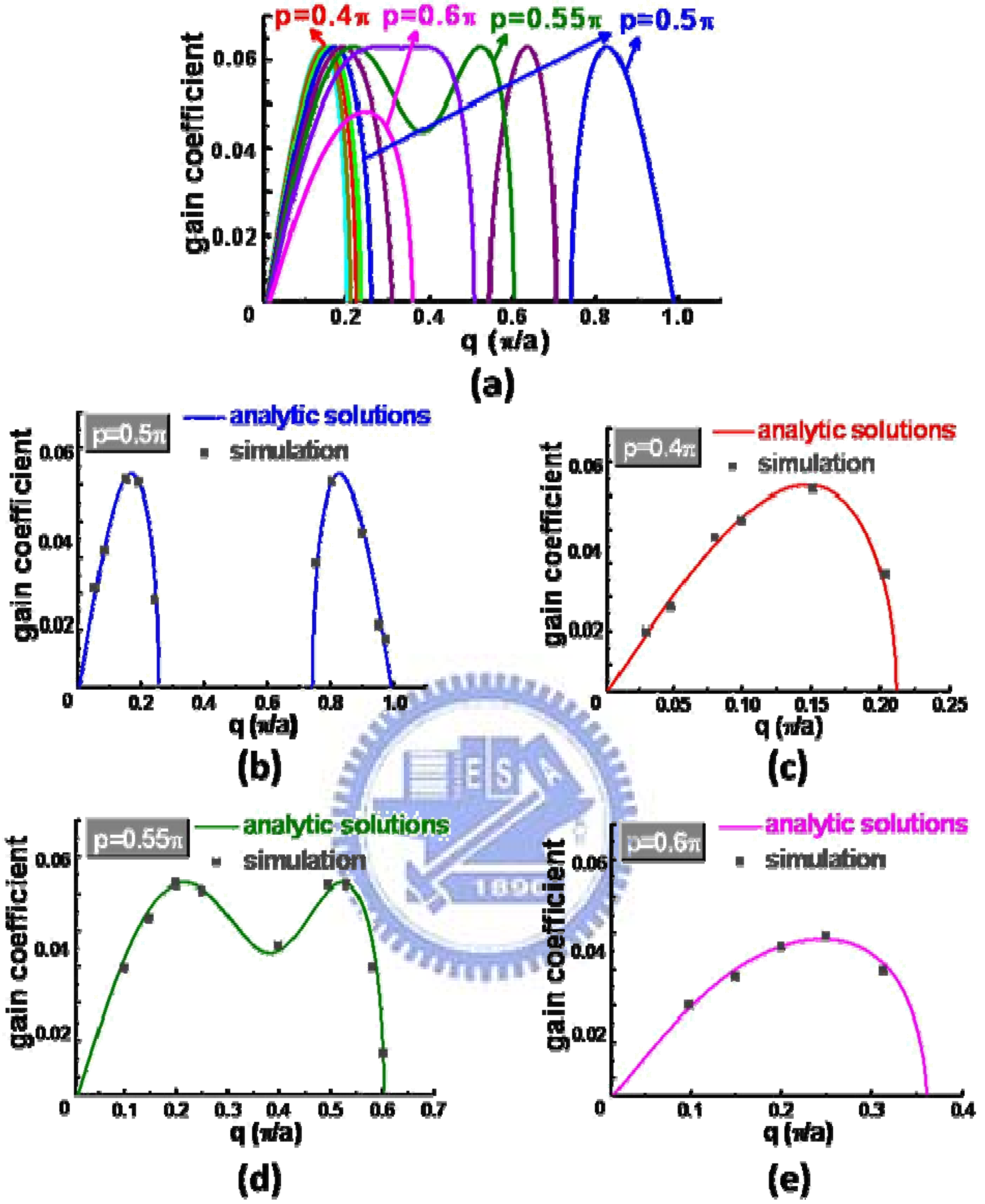

Fig. 3.19 Compare the results of analytic solution and simulation with different p's indicated in the figure.

3.3 Soliton propagation

To follow the discussion in MI, we observe propagating behaviors of initial pulses which are obtained by MI in three cases. Figures 3.20, 3.21, 3.22, and 3.23 show the processes of pulse propagation in these three cases. In case Ⅰ (see Fig. 3.20), solitons and dispersive waves were separated at beginning and after propagation a certain time, we got two solitons. Fourier transforming the pulse, we found the spectrum developed into two solitons with central frequencies of $k_1 = 0.22\pi$ and $k_2 = 0.46\pi$.

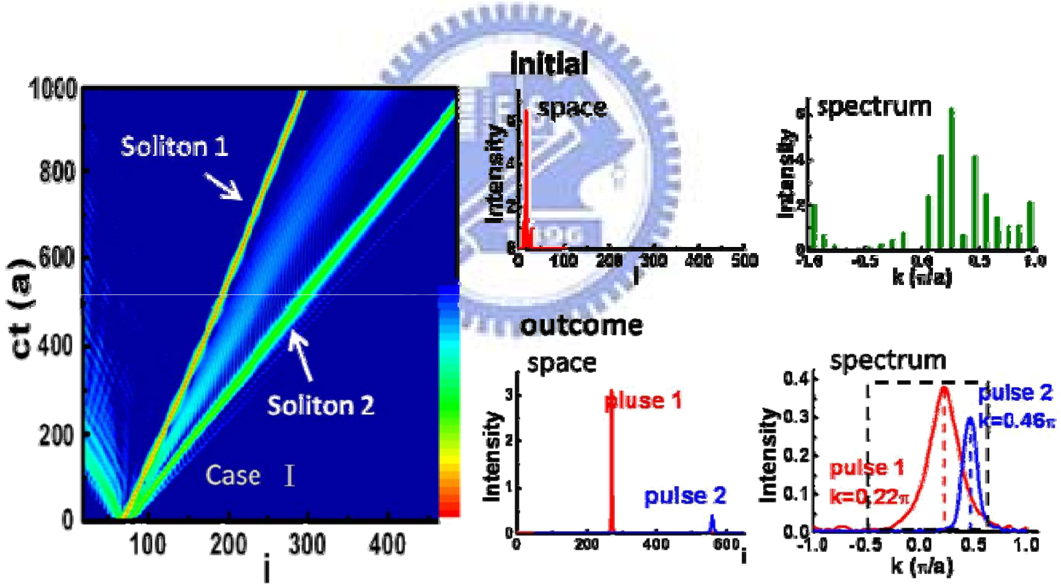

Fig. 3.20 Case Ⅰ ($p = 0.4\pi$, $q = 0.1\pi$): the variation in space and spectrum.

In case Ⅱ, because of two gain areas, we discuss them by two pictures, Figs. 3.21 and 3.22, and we will find their propagating behaviors are quite similar. Soliton 1 and soliton 2 propagated with dispersive waves and tried to fling them unceasingly before pure solitons being formed. The central frequencies of solitons are $k_1 = 0.22\pi$

and k_2= 0.46π from initial condition of p = 0.5π and q = 0.2π; whereas, the central frequencies are in k_1= 0.35π and k_2= 0.5π for another initial condition, p=0.5π and q=0.9π.

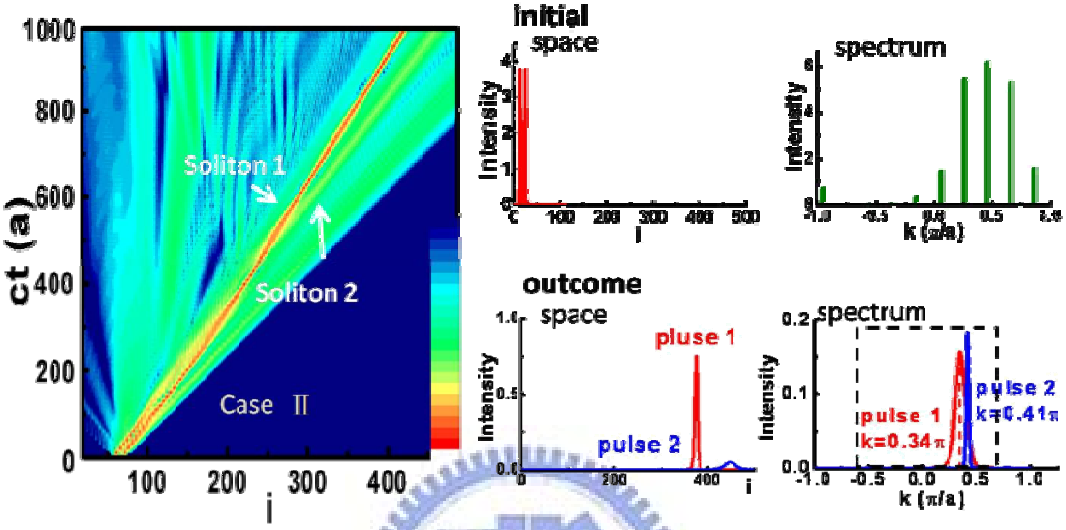

Fig. 3.21 Case Ⅱ (p=0.5π, q=0.2π): the variation of soliton propagation in space and spectrum.

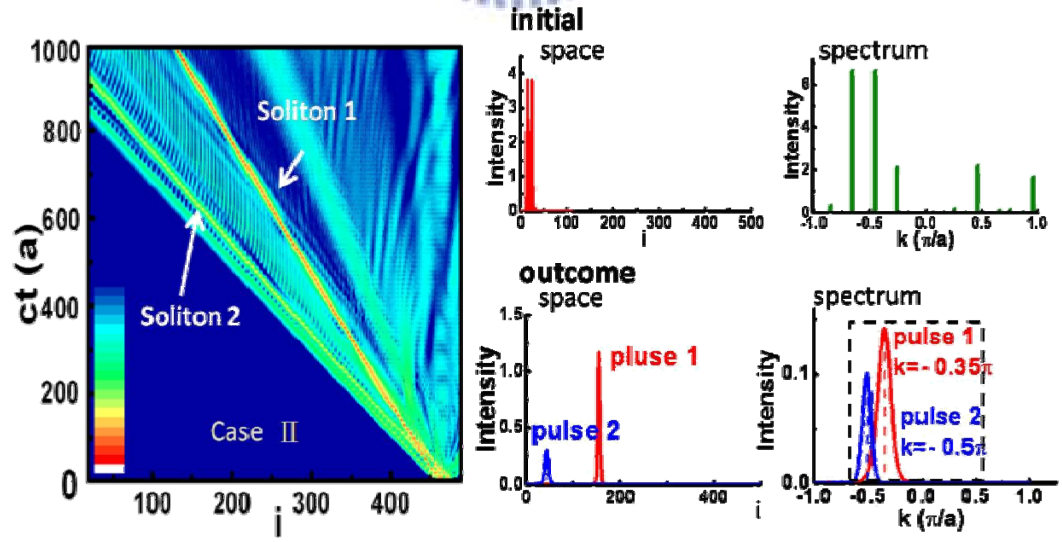

Fig. 3.22 Case Ⅱ (p=0.5π, q=0.9π): the variation of soliton propagation in space and spectrum.

In caseⅢ (see Fig. 23), soliton 1 was formed earlier than soliton 2. During the first half of the propagation, solitons didn't separate from dispersive waves absolutely but became independent finally with central frequencies of solitons at $k_1 = 0.3\pi$ and $k_2 = 0.46\pi$.

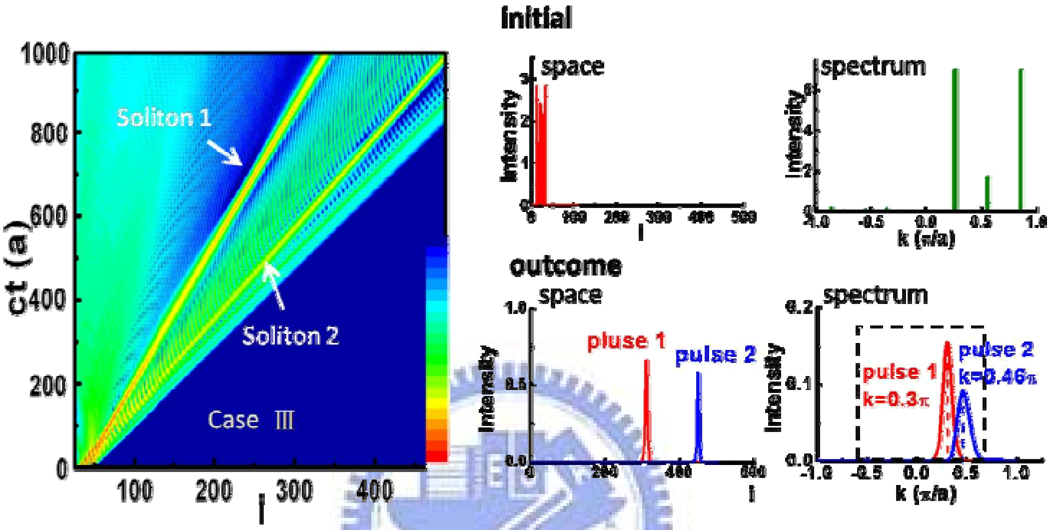

Fig. 3.23 CaseⅢ ($p=0.6\pi$, $q=0.3\pi$): the variation of soliton propagation in space and spectrum.

Now we summarize the soliton propagations in these three cases. In order to explain the propagating behaviors, we broached the group velocity (V_g), the 2nd order and the 3rd order dispersions (β_2, β_3) to help with our understanding. From Fig. 3.24, we can find: (1) All central frequencies located in the region of $0 < k \leq 0.63\pi$, where the dispersion (β_2) is positive, will be compensated by the nonlinear effect ($\gamma < 0$). (2) Becuse β_2 is almost a constant (0.3) and β_3 almost equals 0 in $0 < k < 0.37\pi$, where is a favorate condition for forming broad-band solitons. (3) Solitons 1 in all cases are stable with larger amplitude and shorter pulse width in $0 < k < 0.37\pi$. (4)

Solitons 2 contain smaller β_2 but larger $|\beta_3|$. In order to balance the reduction of β_2, the intensity ($|a_0|^2$ in Eq. 3.2) should diminish to reduce the nonlinear effect. In addition, the increasing high order dispersion $|\beta_3|$ is restrained from narrowing bandwidth Δk (see Eq. 3.1).

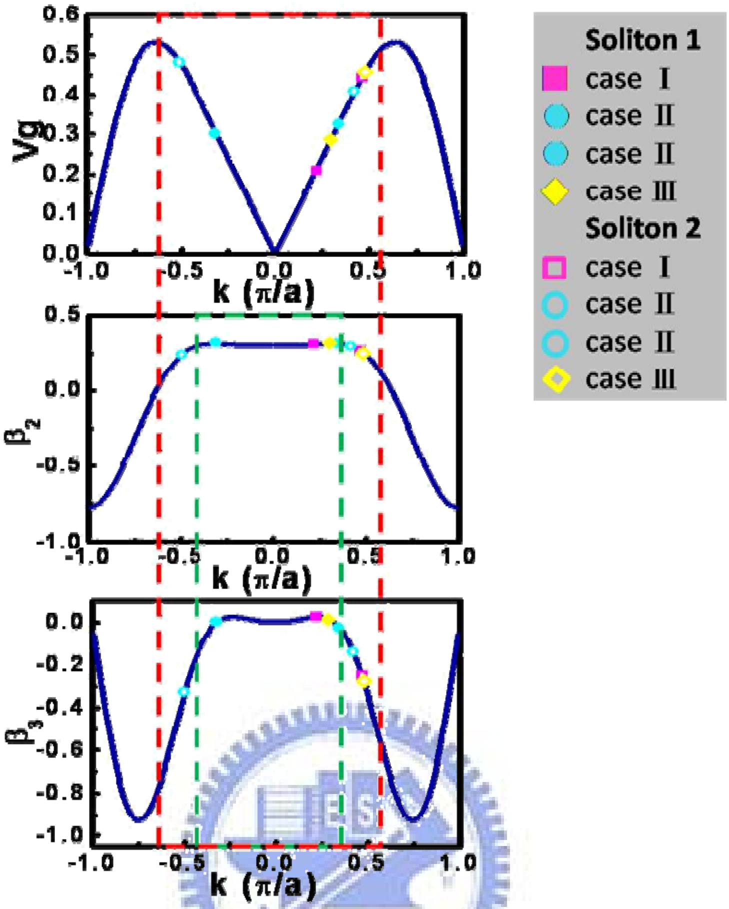

Fig. 3.24 the profiles of V_g, β_2, and β_3.

	Case Ⅰ (p=0.4π, q=0.1π)				CaseⅢ (p=0.6π, q=0.3π)			
	k (π/a)	V_g (c)	β_2	β_3	k (π/a)	V_g (c)	β_2	β_3
Soliton 1	0.22	0.208	0.3	0.026	0.3	0.28	0.3	0.01
Soliton 2	0.47	0.447	0.275	-0.25	0.48	0.45	0.25	-0.28
	CaseⅡ (p=0.5π, q=0.2π)				CaseⅡ (p=0.5π, q=0.9π)			
	k (π/a)	V_g (c)	β_2	β_3	k (π/a)	V_g (c)	β_2	β_3
Soliton 1	0.34	0.325	0.3	-0.02	-0.31	0.3	0.3	-0.004
Soliton 2	0.42	0.4	0.283	-0.14	-0.5	0.5	0.26	-0.33

From the dispersion relation:

$$\frac{1}{2}\Delta k^2\beta_2 + \frac{1}{6}\Delta k^3\beta_3 = \frac{1}{2}\Delta k^2(\beta_2 + \frac{1}{3}\Delta k\beta_3) \quad , \tag{3.1}$$

and Kerr effect:

$$n = n_0 + n_2|a_0|^2, \tag{3.2}$$

one can calculate the soliton number:

$$N^2 = \frac{\gamma P_0 T_0^2}{|\beta_2|}. \tag{3.3}$$

For the sake of thoroughly understanding the effects of different powers P_0 and frequencies k on soliton propagation, we choose a stable soliton pulse and change P_0 and k respectively to observe how the solitons propagate along. First, we use k = 0.22π, 0.32π, and 0.5π (see Fig. 3.25). We found the wave pattern and central frequency nearly didn't change if k = 0.22π or 0.32π. However, the wave pattern broadened and bandwidth became narrower for k = 0.5π in order to diminish the high order dispersion (see Eq. 3.1). Next, we discuss the variable power, P_0, $5P_0$, and $15P_0$ and their central frequencies all fix in k=0.22π. From Fig. 3.26, the initial soliton pulse was separated into several solitons because of increasing intensity and the number of solitons can also be forecasted by Eq. 3.3. Note that, the separated solitons are all in the region of $0 < k \leq 0.63\pi$.

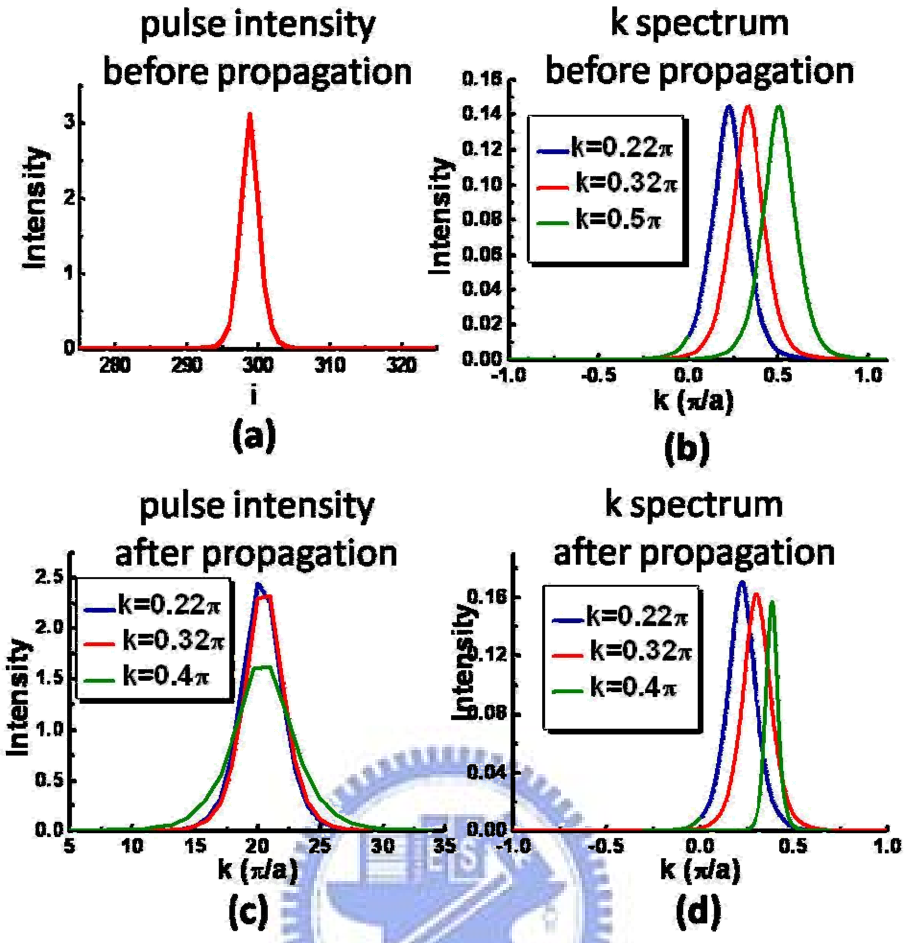

Fig. 3.25 The soliton propagation in space and corresponding spectra for various central spatial frequency of 0.22π, 0.32π, and 0.5π

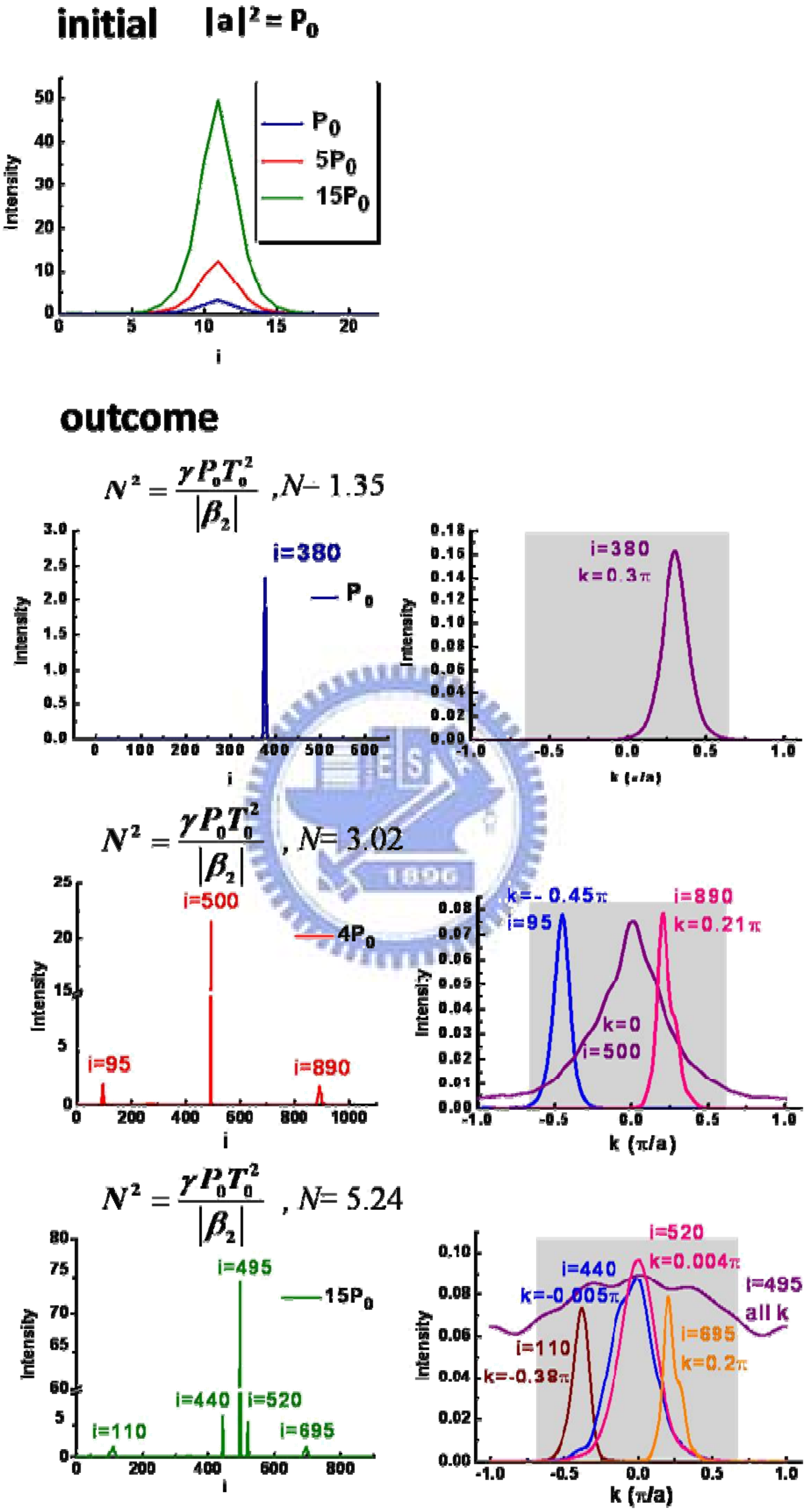

Fig. 3.26 The soliton propagation in space and corresponding spectra for various intensity P_0 for p= 0.22π, 0.32π, and 0.5π.

3.4 Summary

In this chapter, we have proven that using extended NLSE to describe propagating behaviors in nonlinear PCW is essential and we also got the conditions of inducing MI. By solving extended NLSE, we can find a new phenomenon that gain suppression happens in extended NLSE in $0.49\pi < p < 0.6\pi$ for square-array PCW and $0.48\pi < p < 0.51\pi$ for hexagonal-array PCW under $\gamma < 0$. On the other hand, according to the spectrum distribution after modulation instability, we know the soliton chain still contain the dispersive wave. In addition, it's worth to say that the results of analytic solution and simulation are the same.

After propagating a long distance to get rid of dispersive waves, the initial pulses from MI become real solitons and their variations during propagation are independent of the initial conditions of MI. Besides, we can summarize the conditions of soliton formation and some particular behaviors in soliton propagation through our simulation. Moreover, after analyzing soliton propagation, we find that $0<k<0.37\pi$ is a good condition to form broad-band solitons in our simulated cases and the number of solitons can also be forecasted by $N^2 = \frac{\gamma P_0 T_0^2}{|\beta_2|}$ in discrete soliton propagation.

Chapter 4 Conclusion and Future works

4.1 Conclusion

Because the distance between two defects of the consequent PCWs are very short, we shouldn't neglect the coupling effects of several near-neighbor defects. The coupling effects must be considered up to the 3rd nearest-neighbor (NN) defect and it is required to use extended nonlinear Schrödinger equation (NLSE) to describe nonlinear propagation in photonic crystal waveguides (PCWs). According to this extended NLSE, modulation (MI) and MI gain can be analytically determined and there are some different consequences between extended NLSE and NLSE. We found that MI gain in extended NLSE depends upon the incident carrier spatial frequency p, but it is not in NLSE. Besides, gain suppression happens in extended NLSE in $0.49\,\pi < p < 0.6\,\pi$ for square-array PCW and $0.48\,\pi < p < 0.51\,\pi$ for hexagonal-array PCW under $\gamma < 0$.

In order to test and verify the analytic solution, we used the fourth order Runge-Kutta method to solve the extended NLSE. We observed MI and soliton propagation in the spatial and time domains. The results of simulated MI gain are consistent with analytic solutions. The larger MI gain, the easier is to form soliton chain. After analyzing solitons propagation, we found that $0 < k < 0.37\,\pi$ is a favorate condition to form broad-band soliton and the number of solitons can also be forecasted by $N^2 = \frac{\gamma P_0 T_0^2}{|\beta_2|}$ in discrete soliton propagation.

4.2 Future works

We have derived and examined MI gain profiles obtained by using extended NLSE that shows quite different behavior as using NLSE. After analyzing MI and soliton propagation in $\gamma < 0$, we will also investigate the case of $\gamma > 0$, which have anomalous gain profiles with gain suppression at low frequency region. Besides, we will use FDTD method to confirm these results discussed above. On the other hand, we can discuss other structures of PCWs, e.g., hexagonal- array PCW, and compare the results of these different structural arrangements. Moreover, the study of extended NLSE have many applications, for example, it can be applied for the coupled nonlinear PCWs for all-optical switching.

References

[1] E. Yablonovitch, **Phys. Rev. Lett. 58, 2059** (1987).

[2] J. D. Joannopoulos, R. D. Meade, and J. N. Winn, ***Photonic Crystals: Molding the Flow of Light*** (Princeton U. Press, Princeton, N.J., 1995).

[3] A. Mekis, J. C. Chen, I. Kurland, S. Fan, P. R. Villeneuve, and J. D. Joannopoulos, **Phys. Rev. Lett. 77, 3787** (1996).

[4] M. Tokushima, H. Kosaka, A. Tomita, and H. Yamada, **Appl. Phys. Lett. 76, 952** (2000).

[5] S. Y. Lin, E. Chow, J. Bur, S. G. Johnson, and J. D. Joannopolous, **Opt. Lett. 27, 1400** (2002).

[6] K. Hosomi and T. Katsuyama, **IEEE J. Quantum Electron. 38, 825** (2002).

[7] Sulem C and Sulem P L, ***The Nonlinear Schrödinger Equation*** (New York: Springer, 1999).

[8] Benjamin T B and Feir J E, **J. Fluid Mech. 27, 417** (1967).

[9] Ostrovskii L A, **Sov. Phys.—JETP 24, 797** (1969).

[10] Hasegawa A and Kodama Y, ***Solitons in Optical Communications*** *(Oxford: Clarendon, 1995).*

[11] Taniuti T and Washimi H, **Phys. Rev. Lett. 21, 209** (1968); Hasegawa A, **Phys. Rev. Lett. 24, 1165** (1970)

[12] For a recent discussion see e.g., Hammack J L, Henderson D M and Segur H, ***Deep-water waves with persistent, two-dimensional surface patterns*** *(and references therein) Preprint* *http://www.math.psu.edu/dmh/FRG/* (2003)

[13] Peyrard M, Dauxois T, Hoyet H and Willis C R, **Physica D 68, 104** (1993)

[14] Christodoulides D N and Joseph R I, **Opt. Lett. 13, 794** (1988)

[15] Morandotti R, Peschel U, Aitchison J S, Eisenberg H S and Silberberg Y, **Phys. Rev. Lett. 83, 2726** (1999)

[16] Two recent reviews that summarize 20 years of work on the DNLS equation and related topics are: Kevrekidis P G, Rasmussen K Ø and Bishop A R, **Int. J. Mod. Phys. B 15, 2833** (2000); Eilbeck J C and Johansson M, ***Proc. of the 3rd Conf: Localization and Energy Transfer in Nonlinear Systems*** (2003).

[17] Kivshar Yu S and Peyrard M, **Phys. Rev. A 46, 3198** (1992)

[18] R. Y. Chiao, E. Garmire, and C. H. Townes, **Phys. Rev. Lett. 13, 479** (1964).

[19] A. Hasegawa and F. Tappert, **Appl. Phys. Lett. 23, 142** (1973).

[20] L. F. Mollenauer, R. H. Stolen, and J. P. Gorden, **Phys. Rev. Lett. 45, 1095** (1980).

[21] C. Pare, A. Villeneuve, and S. LaRochelle, **Opt. Commun. 160, 130** (1999).

[22] B. J. Eggleton, G. Lenz, and N. M. Litchinitser, Fiber and Integrated optics **19**, 383 (2000).

[23] A. Hasegawa, **IEEE. J. Sel. Top. Quant. 6, 1161** (2000); **Chaos, 10, 475** (2000); **Physics of Plasmas 8, 1763** (2001).

[24] N. Stefanou and A. Modinos, **Phys. Rev. B 57, 12127** (1998).

[25] A. Yariv, Y. Xu, R. K. Lee, and A. Scherer, **Opt. Lett. 24, 711** (1999).

[26] M. Bayindir, B. Temelkuran, and E. Ozbay, **Phys. Rev. Lett. 84, 2140** (2000).

[27] M. Bayindir, B. Temelkuran, and E. Ozbay, **Phys. Rev. B 61, R11855** (2000).

[28] M. Bayindir and E. Ozbay, **Phys. Rev. B 62, R2247** (2000).

[29] S. Mookherjea and A. Yariv, **Opt. Express 9, 91** (2001), http://www.opticsexpress.org.

[30] Y. Xu, R. K. Lee, and A. Yariv, **J. Opt. Soc. Am. B 17, 387** (2000).

[31] M. Notomi, K. Yamada, A. Shinya, J. Takahashi, C. Takahashi, and I. Yokohama, **Phys. Rev. Lett. 87, 253902** (2001).

[32] F. S. S Chien, J. B. Tu, W. F. Hsieh and S. C. Cheng, **Phys. Rev. B 75, 125113** (2007).

[33] Demetrios N. Christodoulides and Nikos K. Efremidis, **Opt. Lett. 27, 8** (2002).

[34] Yuri S. Kivshar and Govind P. Agrawal, ***Optical Solitons***, (2003).

[35] Z Rapti, P G Kevrekidis, A Smerzi, and A R Bishop, **Phys. B: At. Mol. Opt. Phys. 37, S257–S264** (2004).

[36] J. P. Albert, C. Jouanin, D. Cassagne, and D. Bertho, **Phys. Rev. B 61, 4381** (2000).

[37] Y. R. Shen, ***Principles of Nonlinear Optics*** *(Wiley, New York)* (1984).

[38] P. N. Butcher and D. N. Cotter, ***The Elements of Nonlinear Optics*** *(Cambridge University Press, Cambridge, UK,* 1990*).*

[39] R. W. Boyd, ***Nonlinear Optics*** *(Academic Press, San Diego, CA,* 1992*).*

[40] G. P. Agrawal, ***Nonlinear Fiber Optics, 3rd ed.*** *(Academic, San Diego, CA,* 2001*).*

[41] William H. Press, Saul A. Teukolsky, William T. Vetterling, Brian P. Flannery, ***Numerical Recipes in Fortran 77,*** **2nd ed.** *(Cambridge University Press,* 1992*)*